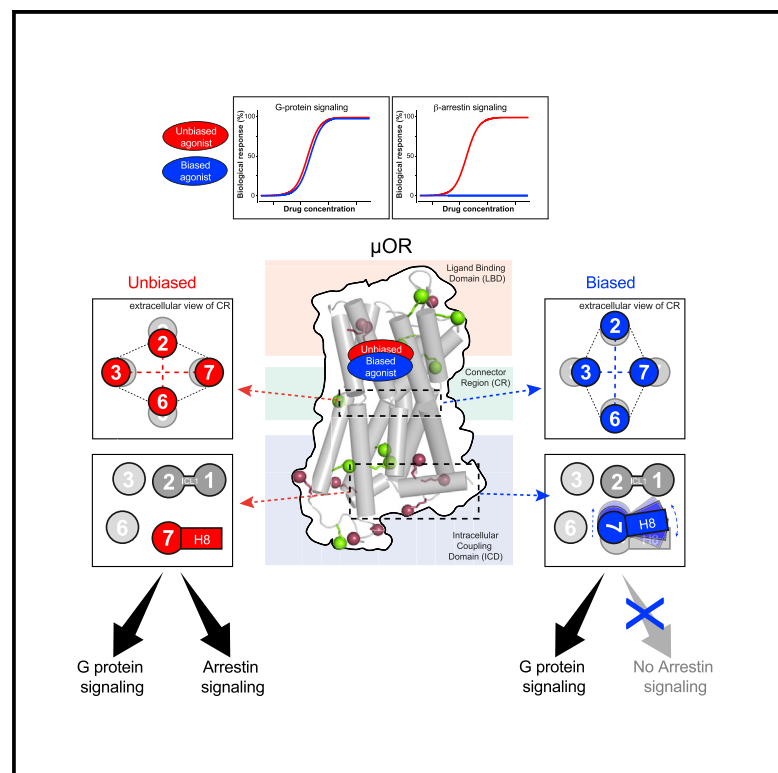# Molecular insights into the biased signaling mechanism of the μ-opioid receptor

Graphical abstract

Authors

Xiaojing Cong, Damien Maurel, Hélène Déméné, ..., Jérôme Golebiowski, Sébastien Granier, Rémy Sounier

Correspondence

sebastien.granier@igf.cnrs.fr (S.G.), remy.sounier@igf.cnrs.fr (R.S.)

In brief

Biased ligands of GPCRs offer new drug design strategies to enhance beneficial drug actions while reducing side effects. Cong et al. combined molecular simulations, NMR spectroscopy, and functional assays to uncover the molecular mechanism of ligand bias in the μ-opioid receptor, which provides structural basis for designing better opioid analgesics.

Highlights

- NMR and MD simulations help define the molecular mechanisms of μOR-biased signaling

- Biased, unbiased, and partial agonists stabilize different μOR conformations

- Biased agonists stabilize specific conformations in the TM7, ICL1, and H8 domains

- The bias in conformation persists after binding to a G protein mimetic nanobody

CellPress

Article

Molecular insights into the biased signaling mechanism of the μ-opioid receptor

Xiaojing Cong,[1,5] Damien Maurel,[1,5] Hélène Déméné,[2] Ieva Vasiliauskaité-Brooks,[1] Joanna Hagelberger,[1] Fanny Peysson,[1] Julie Saint-Paul,[1] Jérôme Golebiowski,[3,4] Sébastien Granier,[1,*] and Rémy Sounier[1,6,*]

[1]Institut de Génomique Fonctionnelle, CNRS UMR-5203 INSERM U1191, University of Montpellier, 34000 Montpellier, France
[2]Centre de Biochimie Structurale, CNRS UMR 5048-INSERM 1054, University of Montpellier, 29 rue de Navacelles, 34090 Montpellier Cedex, France
[3]Université Côte d'Azur, CNRS, Institute of Chemistry of Nice UMR7272, 06108 Nice, France
[4]Department of Brain and Cognitive Sciences, Daegu Gyeongbuk Institute of Science and Technology, Daegu 711-873, South Korea
[5]These authors contributed equally
[6]Lead contact
*Correspondence: sebastien.granier@igf.cnrs.fr (S.G.), remy.sounier@igf.cnrs.fr (R.S.)
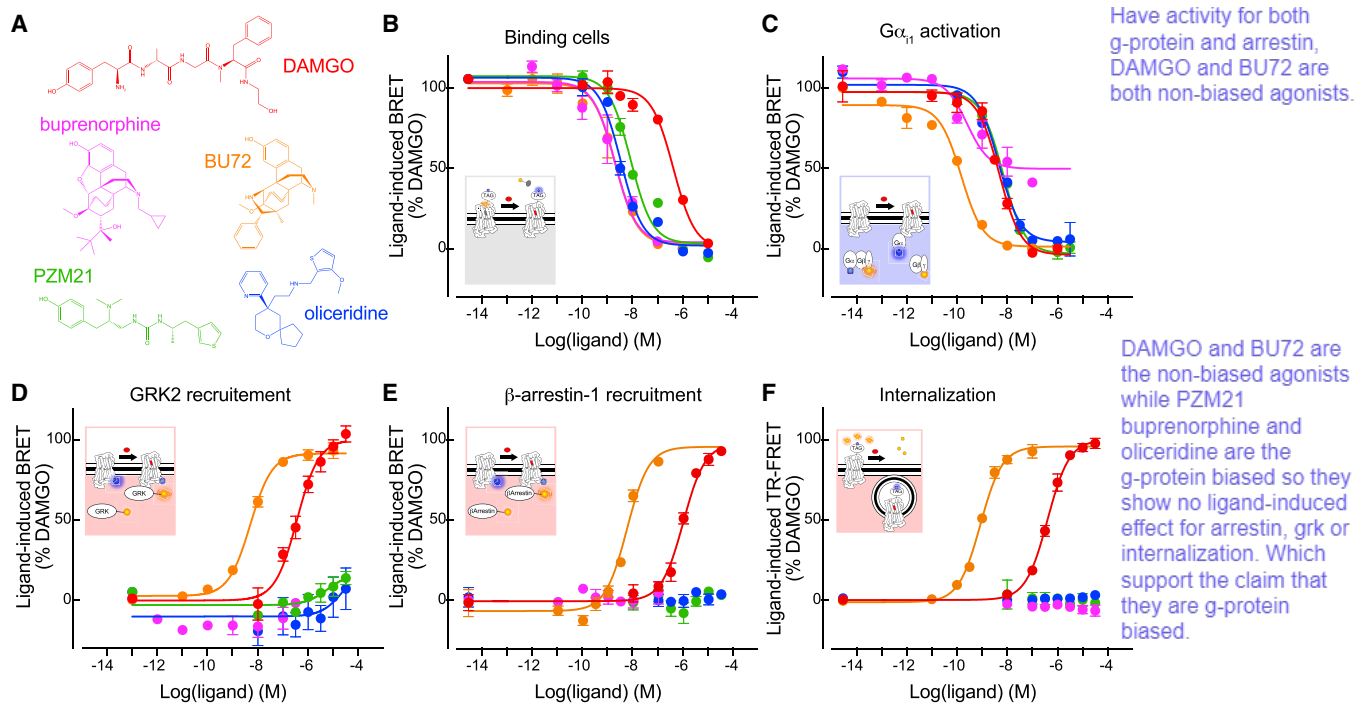https://doi.org/10.1016/j.molcel.2021.07.033

SUMMARY

GPCR functional selectivity opens new opportunities for the design of safer drugs. Ligands orchestrate GPCR signaling cascades by modulating the receptor conformational landscape. Our study provides insights into the dynamic mechanism enabling opioid ligands to preferentially activate the G protein over the β-arrestin pathways through the μ-opioid receptor (μOR). We combine functional assays in living cells, solution NMR spectroscopy, and enhanced-sampling molecular dynamic simulations to identify the specific μOR conformations induced by G protein-biased agonists. In particular, we describe the dynamic and allosteric communications between the ligand-binding pocket and the receptor intracellular domains, through conserved motifs in class A GPCRs. Most strikingly, the biased agonists trigger μOR conformational changes in the intracellular loop 1 and helix 8 domains, which may impair β-arrestin binding or signaling. The findings may apply to other GPCR families and provide key molecular information that could facilitate the design of biased ligands.

INTRODUCTION

Cell signaling relies on second messenger systems that are modulated by G protein-coupled receptors (GPCRs) in a ligand-specific manner. GPCRs are known for the complexity of their signaling pathways and conformational landscape. Ligands may preferentially activate or inhibit distinct signaling pathways by changing the conformations of the GPCR (Weis and Kobilka, 2018). This is known as functional selectivity (or ligand bias), which provides fine regulations of GPCR functions and new drug design opportunities. Functional selectivity of the μ-opioid receptor (μOR) is among the most studied, in a global effort to develop safer analgesics. Opioid analgesics are efficacious and inexpensive, but their severe side effects caused the ongoing opioid epidemic beginning in the 1990s. A number of studies from 2005 to 2010 associated major opioid side effects with the β-arrestin signaling pathways (reviewed in Raehal et al., 2011), which has driven more than a decade of research on G protein-biased μOR agonists. This led to the discovery of oliceridine (TRV130) (DeWire et al., 2013) and PZM21 (Manglik et al., 2016), two G protein-biased agonists showing fewer side effects than morphine in early studies. Oliceridine was approved

by the U.S. Food and Drug Administration (FDA) in 2020 for pain management, but it still has typical opioid side effects, such as nausea, vomiting, dizziness, headache, and constipation. There are high expectations for PZM21, which outperformed oliceridine and morphine in mice (Manglik et al., 2016). Nevertheless, recent findings argue that G-protein selectivity may improve analgesia and tolerance but not necessarily the side effects (Kliewer et al., 2019). Opioid-induced respiratory depression and constipation could be independent of β-arrestin signaling (Kliewer et al., 2020). It was suggested that the favorable therapeutic profiles of oliceridine and PZM21 are due to low efficacy rather than functional selectivity (Gillis et al., 2020; Yudin and Rohacs, 2019). Yet G-protein selectivity correlates with broader therapeutic windows, enabling better separations of the beneficial and adverse opioid effects (Schmid et al., 2017). A potential explanation for these discrepancies is the weak selectivity of these ligands compared with the complexity of the GPCR signaling network (Conibear and Kelly, 2019). The diversity of the systems used may also be a source of inconsistency. There is a pressing need for strongly biased and highly specific ligands, to probe the μOR signaling network for more insights. Finding such probes demands understanding the molecular mechanism

Figure 1. Functional characterizations of the μOR agonists

Text annotations accompanying figure:

Have activity for both g-protein and arrestin, DAMGO and BU72 are both non-biased agonists.

DAMGO and BU72 are the non-biased agonists while PZM21 buprenorphine and oliceridine are the g-protein biased so they show no ligand-induced effect for arrestin, grk or internalization. Which support the claim that they are g-protein biased.

Figure 1. Functional characterizations of the μOR agonists
(A) Chemical structures of the five agonists.
(B–F) Dose-dependent response curves of the agonists in (B) competitive binding against fluorescent naltrexone in living cells, (C) activating $G\alpha_{i1}$, (D) inducing GRK2 recruitment, (E) inducing β-arrestin1 recruitment, and (F) inducing μOR internalization. Color code in (B)–(F) is the same as in (A). Data shown are mean ± SD of a representative experiment performed in triplicates normalized to the maximal response induced by DAMGO and fitted using an operational model of agonism. See also Table S1.

of functional selectivity, which is intrinsic to the GPCR. However, GPCRs are not static on/off switches but complex molecular machines that operate through strictly regulated motions (Weis and Kobilka, 2018). Functional selectivity relies on the dynamic equilibrium of GPCR conformations, which is so far poorly understood.

X-ray crystallography and Cryo-electron microscopy (cryo-EM) have successfully captured inactive and active μOR states (Huang et al., 2015; Koehl et al., 2018; Manglik et al., 2012). Yet they represent essentially a few snapshots of the vast landscape of GPCR conformations. The active states of ternary complexes exhibit a large outward displacement of the transmembrane helix 6 (TM6), which requires stabilization by G proteins or G protein mimetics (reviewed in Weis and Kobilka, 2018). Conformational changes induced by ligand binding, however, are very subtle and dynamic, as revealed by recent nuclear magnetic resonance (NMR) studies on the β2-adrenergic receptor (β2AR) (Manglik et al., 2015; Nygaard et al., 2013) and on μOR (Okude et al., 2015; Sounier et al., 2015). Agonist binding initiate slight conformational changes in the ligand-binding domain (LBD), sufficient to trigger long-range conformational changes via the connector region (CR) until the intracellular coupling domains (ICDs), in an allosteric and dynamic manner. Signaling partners (e.g., G proteins or β-arrestins) couple to the activated ICD and induce further large-scale opening of ICD to a fully active state. This activation process is common in various GPCRs such as the leuko-

(margin notes: "as we observed in the pdbs"; "check on these references")

triene B4 receptor 2 (LTB4-R2) (Casiraghi et al., 2016), the β1-adrenergic receptor (β1AR) (Isogai et al., 2016), the adenosine A_{2A} receptor ($A_{2A}R$) (Clark et al., 2017; Eddy et al., 2018; Ye et al., 2016), and the muscarinic M2 receptor (M_2R) (Xu et al., 2019). However, detailed activation dynamics, especially the mechanism of functional selectivity, are difficult to capture by X-ray crystallography or cryo-EM. NMR spectroscopy has proved to be particularly suitable for monitoring subtle dynamic conformational transitions during GPCR activation (Kofuku et al., 2014; Liang et al., 2018; Shimada et al., 2019). Likewise, molecular dynamics (MD) simulations have provided atomic-level detailed insights (Latorraca et al., 2017), such as the long-timescale MD of β2AR deactivation and activation (Dror et al., 2011; Kohlhoff et al., 2014), as well as enhanced-sampling MD of the activation of M_2R (Miao et al., 2013) and $A_{2A}R$ (Lovera et al., 2019). Here, we combined a thorough functional investigation of agonists, NMR spectroscopy, and MD simulations to obtain atomic-level descriptions of μOR agonism. To this end, we established a dual-isotope labeling NMR scheme for μOR on the basis of our previous study (Sounier et al., 2015). For MD, we used the REST2 enhanced-sampling scheme (REST2-MD; see Method details in STAR Methods), which has proved efficient in monitoring GPCR activation (Cong et al., 2018, 2019; Cong and Golebiowski, 2018; Sena et al., 2017).

We studied five chemically distinct μOR agonists (Figure 1A): DAMGO, a well-characterized μOR-specific peptide (Emmerson

et al., 1994; Handa et al., 1981); buprenorphine, a semi-synthetic thebaine analog and partial agonist (Cowan et al., 1977a, 1977b); BU72, a potent buprenorphine derivative (Neilan et al., 2004); and the aforementioned biased agonists oliceridine and PZM21. By comparing the effects of these agonists on the μOR conformational dynamics, we provide here insights into the molecular mechanism of μOR functional selectivity.

RESULTS

Opioids signaling in living cells

We first characterized the functional profiles of the five opioids in cell-based assays for their abilities to bind the target, to activate G proteins (Gi/o) and GPCR kinase 2/5 (GRK2/5), to recruit β-arrestins 1 and 2, and to trigger μOR internalization. Using advanced fluorescence methods, we probed (1) competitive ligand binding to the target cells and μOR against naltrexone, (2) dissociation of the G protein heterotrimer, (3) ligand-induced μOR interactions with GRK2/5 or (4) with β-arrestins-1/2, and (5) diminution of cell-surface μORs (internalization) (Figures 1B–1F and S1; Table S1).

All five opioids behaved as agonists in the Gi$_{1-2-3}$ and Go$_{a-b}$ activation assays (Figures 1C and S1A–S1D). PZM21 and oliceridine behaved as full agonists in our G protein assays, similar to the data of Ehrlich et al. (2019) using the same assays. However, other studies described them as partial agonists (Gillis et al., 2020; Hill et al., 2018; Yudin and Rohacs, 2019). These discrepancies highlight how functional assay outcomes may vary because of overexpression, assay conditions, assay readout amplification, or the presence of high receptor reserve (Kelly, 2013), whereby an agonist may achieve maximal response by occupying only a fraction of the existing receptor population. Compared with DAMGO (our reference ligand), buprenorphine was the only partial agonist in our assays, showing 63% ± 9% to 83% ± 10% of efficacy even at saturating concentration (Figures 1B, 1C, and S1A–S1D; Table S1). This agrees with previous cell signaling assays (Ehrlich et al., 2019; McPherson et al., 2010; Traynor and Nahorski, 1995). Concerning the recruitments of GRK2/5 and β-arrestin-1/2, and μOR internalization, DAMGO and BU72 showed comparable efficacies, with the latter being more potent, whereas oliceridine, PZM21, and buprenorphine showed nearly no response (Figures 1D–1F and S1E; Table S1). Therefore, oliceridine, PZM21, and buprenorphine were clearly G protein biased. Note that the bias factors could not be determined, as no transduction coefficient (log[τ/K_A]) values could be calculated, because of their lack of measurable response in the β-arrestin-1/2, GRK2/5, and internalization assays. Because our functional assays were to be compared with the NMR and REST2-MD data, which provide rather qualitative information, we did not further quantify the ligands' efficacy or bias. For the purpose of this study, we simply classified DAMGO and BU72 as unbiased full agonists, oliceridine and PZM21 as G protein-biased full agonists, and buprenorphine as a G protein-biased partial agonist.

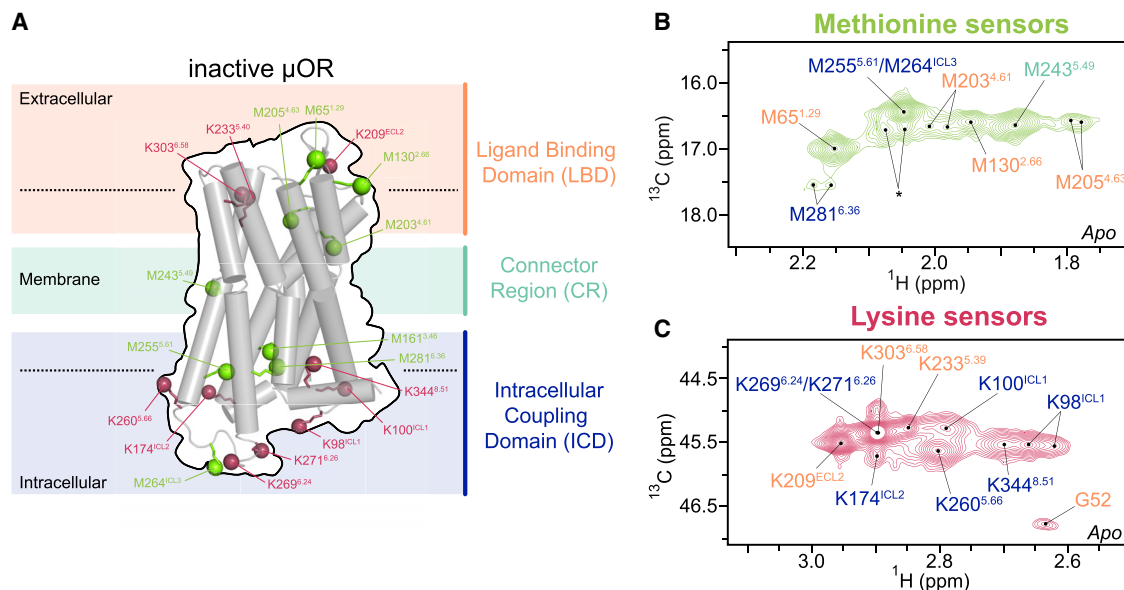### Development of multidomain NMR sensors for allosteric GPCR motions

We used a previously established mouse μOR construct for NMR spectroscopy, which contained an M72$^{1.36}$T mutation

(superscript refers to the Ballesteros-Weinstein numbering) that increased the expression level (Sounier et al., 2015) and reduced the NMR peak overlaps. The N terminus was truncated before residue G52. This μOR construct maintained intact μOR functions and was stable for the duration of the NMR experiments (Sounier et al., 2015) (Figures S1F and S2A). Our previous approach used lysine sensors to probe μOR motions in the solvent-accessible domains (Sounier et al., 2015). Here we developed a dual-isotope methyl labeling scheme to monitor the solvent-accessible domains and the 7-transmembrane helices (7TM) simultaneously. For this purpose, we introduced NMR-active ^{13}C probes into methionines (biosynthetically) and lysines (through reductive methylation) of the μOR construct. The heteronuclear multiple-quantum coherence (HMQC) pulse sequences were used to obtain two-dimensional (2D) ^{1}H-^{13}C chemical shift correlation maps (see Method details in STAR Methods). The ^{13}CH$_3$-ε-methionine peak assignments were obtained by mutagenesis of individual methionine residues and the dimethylamine peak assignments from our previous work (Sounier et al., 2015). We unambiguously assigned 20 sensors in the unliganded (apo) μOR (Figures 2A–2C, S2, and S3; see STAR Methods). The G52 backbone amine was at the N terminus. Three lysines (K209^{ECL2}, K233$^{5.39}$, and K303$^{6.58}$), and four methionines (M65$^{1.29}$, M130$^{2.66}$, M203$^{4.61}$, and M205$^{4.63}$) were located in the LBD. In the ICD, seven lysines (K98^{ICL1}, K100^{ICL1}, K174^{ICL2}, K260$^{5.66}$, K269$^{6.24}$, K271$^{6.26}$, and K344$^{8.51}$) and four methionines (M161$^{3.46}$, M255$^{5.61}$, M264^{ICL3}, and M281$^{6.36}$) were assigned. Only one methionine M243$^{5.49}$ was assigned to the CR.

To monitor agonist-induced μOR activation, we collected the HMQC spectra of μOR bound to each agonist, with and without the G protein-mimetic nanobody Nb33 (Figures 2A–2C and S2D–S2F). Nb33 was necessary to reach the fully active state of μOR (Sounier et al., 2015), whereas without Nb33 we obtained the effects of the agonist binding, which more likely reflect the intrinsic mechanism of ligand bias. Taking into account the receptor concentration and the ligand depletion (Hulme and Trevethick, 2010), we estimated that 99% of the μORs should be in complexes during the NMR measurements.

Conformational link between the LBD and the intracellular partner protein binding site

Upon binding of the agonists alone, the LBD sensors M65$^{1.29}$ and M205$^{4.63}$ exhibited multiple peaks with different intensities, which varied among the five agonists (Figures S4D, S4E, S4M, and S4N). This indicates intermediate to slow exchanges among multiple conformations of the receptor and/or the agonists on the NMR timescales. The N-terminal sensor G52 showed a remarkable peak appearance for all five agonists (Figures S4G and S4H), which was further increased upon Nb33 binding (Figure S4I). This suggests that ligand binding stabilized the N terminus, which was enhanced upon Nb33 binding. Indeed, the N terminus formed a pocket lid in the crystal structure of BU72-μOR-Nb33 (PDB: 5C1M). Nb33 binding at the ICD also caused spectra changes in the extracellular loop 2 (ECL2) in a ligand-dependent manner (Figures S4A–S4C). These results suggest that (1) Nb33 binding at the ICD has a long-range allosteric modulation of the LBD conformations; (2) Nb33 triggers cooperative interactions among the N terminus, ECL2, and the

Figure 2. Development of multidomain NMR sensors

(A) Location of the NMR sensors in a cartoon representation of μOR in inactive form. The NMR sensors, ε-CH₃ of methionine (green) and ε-NH₂ of lysine (raspberry), are shown as balls, in the ligand-binding domain (LBD; pale orange), the connector region (CR; pale green), and the intracellular coupling domain (ICD; blue).

(B and C) Extracted 2D HMQC spectra of the methionine and lysine sensors, as well as the backbone amine of the N-terminal residue G52, in apo μOR. Asterisk indicates the peak positions of residual resonances of the N-terminal methionine in a small amount of untruncated μOR.

orthosteric pocket; and (3) the agonists alone do not stabilize the fully active state even in the LBD. Importantly, these data are in line with the allosteric link between the LBD and the ICD recently reported for other class A GPCRs (Eddy et al., 2018; Liu et al., 2017, 2019a).

At the G protein binding site (at TM5/ICL3/TM6 in the ICD), the five agonists induced only small conformational changes (Figures S5B, S5F, and S5J). Nevertheless, the small changes were sufficient for the binding of Nb33, which in turn induced large conformational changes in TM5/TM6 as seen in the crystal structures of active μOR (Huang et al., 2015) (Figures S5C, S5G, and S5K). The magnitudes of the changes in the ternary μOR-agonist-Nb33 complexes correlated with the G-protein efficacies of the agonists (Figures S5D and S5H). This suggests that the capacity of an agonist to cooperate with the G proteins allosterically determines its efficacy to activate the canonical G protein signaling pathway.

Biased, unbiased, or partial agonists exhibit different binding poses

To investigate the molecular mechanism of the discrete agonist activities, we performed REST2-MD simulations (see Method details in STAR Methods; Figure S6A) to examine how each agonist modulates the μOR conformational ensemble. All simulations were initiated by docking the agonist to the crystal structure coordinates of μOR in an inactive form (PDB: 4DKL) (Manglik et al., 2012) without Nb33. The REST2-MD reproduced the binding poses of DAMGO and BU72 in the cryo-EM/crystal structures of μOR in active forms (PDB: 6DDE [Koehl et al., 2018] and 5C1M [Huang et al., 2015], respectively; Figure S6B). This

confirmed sufficient conformational sampling by the REST2-MD in our protocol. The biased agonists, oliceridine, PZM21, and buprenorphine, turned out to bind deeper into the CR than DAMGO and BU72. They inserted between W293⁶·⁴⁸ and TM2, whereas DAMGO and BU72 bound on top of W293⁶·⁴⁸ (Figure 3A). The REST2-MD also captured alternative, short-lived binding poses of oliceridine and PZM21, in which the ligands bound on top of W293⁶·⁴⁸ (Figure S6C). These are likely transient poses in the binding process. Indeed, the HMQC spectra in the LBD indicated exchanges between different receptor/ligand conformations for all the five agonists (Figure S4) Whether such transient binding poses contribute to the receptor activation in the ICD is difficult to determine, as the LBD and the ICD are loosely coupled. Therefore, we focus on the ensemble changes in the receptor conformational equilibrium, without interpreting the roles of the transient binding poses.

In the case of buprenorphine, the partial agonist, W293⁶·⁴⁸ switched between two rotamers, whereas the full agonists maintained mostly one of the W293⁶·⁴⁸ rotamers as in apo μOR (Figure 3B). W293⁶·⁴⁸ is part of the conserved CW⁶·⁴⁸xP motif in class A GPCRs, known as the "toggle switch" of receptor activation. It is located at the bottom of the orthosteric pocket, on top of the conserved "PIF" motif (P244⁵·⁵⁰, I155³·⁴⁰, and F289⁶·⁴⁴) in the CR. Together, they form the so-called connector region, which mediates the allosteric communications between the LBD and the ICD (Latorraca et al., 2017). W293⁶·⁴⁸ plays important roles in μOR activation or inhibition (Huang et al., 2015; Yuan et al., 2015). Therefore, the different agonist binding poses with respect to W293⁶·⁴⁸ may be the initial trigger of the different signaling outcomes.
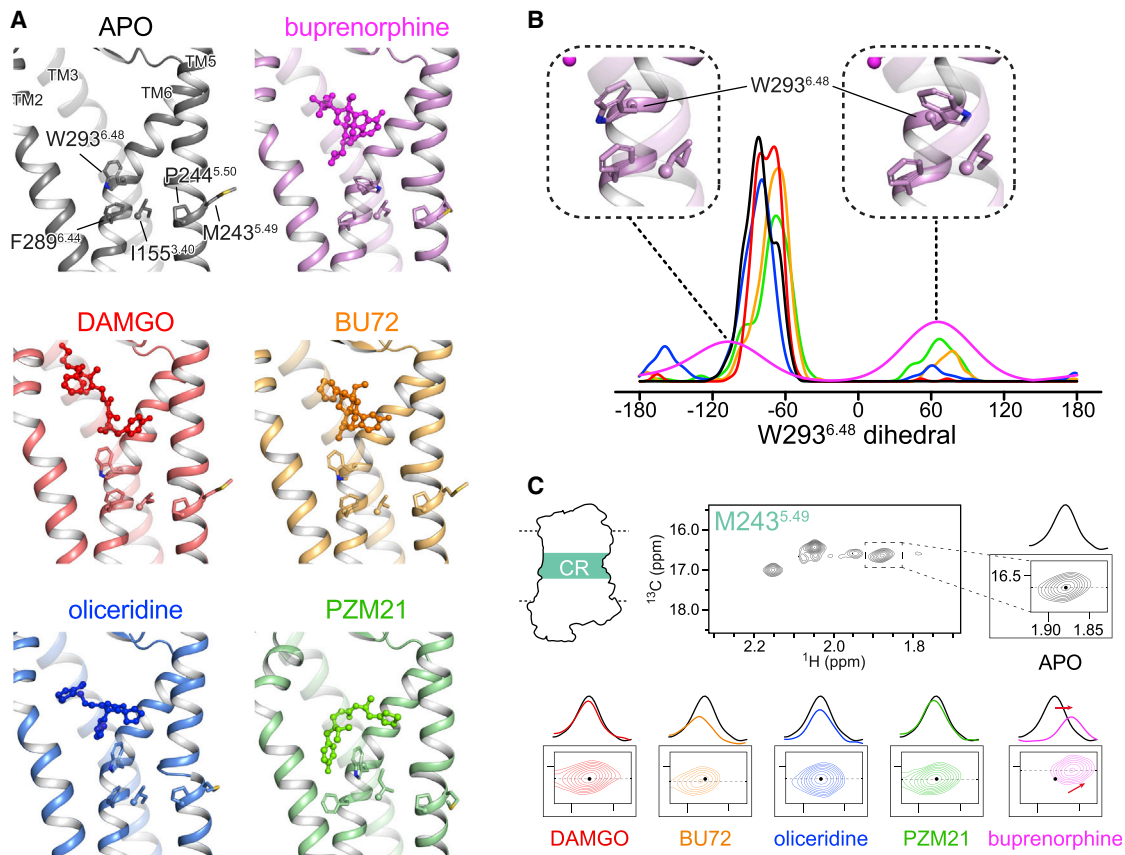
Figure 3. Distinct binding patterns of biased, unbiased, and partial agonists in comparison with NMR

(A) Unbiased agonists (DAMGO and BU72) bind on top of W293$^{6.48}$, whereas biased ones (oliceridine, PZM21, and buprenorphine) insert between W293$^{6.48}$ and TM2. The conserved "PIF" motif (P244$^{5.50}$, I155$^{3.40}$, and F289$^{6.44}$) and the NMR sensor M243$^{5.49}$ in the CR are shown as sticks.

(B) Ligand-dependent rotamers of W293$^{6.48}$, as measured by the distribution of the dihedral angle χ_2 during the REST2-MD simulations.

(C) Extracted HMQC spectra of M243$^{5.49}$ resonances in *apo* μOR (black) and at saturating concentration of DAMGO (red), BU72 (orange), oliceridine (blue), PZM21 (green), and buprenorphine (magenta). Dashed black lines indicate the position of the cross-sections shown above the spectra.

The above REST2-MD observations were confirmed by the NMR sensor M243$^{5.49}$ in the CR. We spotted a distinct pattern in the buprenorphine-μOR complex than in the other systems: the peak of M243$^{5.49}$ shifted up-field in both the ^{1}H and ^{13}C dimensions, as expected from the rotation of W293$^{6.48}$ toward M243$^{5.49}$ upon buprenorphine binding (Figure 3C). Interestingly, during an experiment using the antagonist naloxone, the M243$^{5.49}$ peak shifted slightly in the same directions as in the case of buprenorphine (Figure S2G). The shift is likely associated with some constitutively active conformations in *apo* μOR that were diminished upon naloxone binding. Given the well-documented "toggle switch" role of W293$^{6.48}$ in μOR activation (Huang et al., 2015; Yuan et al., 2015), we conclude that the low efficacy of buprenorphine is associated with its low capability to stabilize the required W293$^{6.48}$ rotameric state for activation.

Conformational changes in the intracellular β-arrestin binding site

The biased agonists oliceridine and PZM21 produced distinct μOR conformations in the lower half of TM7, the intracellular loop 1 (ICL1), and the helix 8 (H8) during the REST2-MD. The simulations revealed an allosteric communication from W293$^{6.48}$ to ICL1 and H8, through the conserved motifs G$^{1.49}$N$^{1.50}$ and N$^{7.49}$P$^{7.50}$xxY$^{7.53}$. Namely, the biased agonists inserted between W293$^{6.48}$ and A117$^{2.53}$ in the CR and split TM6 and TM2, which let TM7 approach TM3 (Figures 4A–4C). The N$^{7.49}$P$^{7.50}$xxY$^{7.53}$ motif in TM7 thus moved toward TM3, away from the G$^{1.49}$N$^{1.50}$ motif in TM1 (Figures 4C–4E). This led to remarkable inward movements of TM7 and H8 toward TM3 in the ICD, closing the cleft between H8 and ICL1 (Figures 5A–5C). In the case of the unbiased agonists (DAMGO and BU72), W293$^{6.48}$ interacted with A117$^{2.53}$, while N$^{7.49}$P$^{7.50}$xxY$^{7.53}$ remained in close contact with G$^{1.49}$N$^{1.50}$. Residues N332$^{7.49}$ and Y336$^{7.53}$ formed a hydrophilic cluster with N86$^{1.50}$ and D114$^{2.50}$. D$^{2.50}$ is the sodium binding site conserved in 90% of non-olfactory class A GPCRs (Katritch et al., 2014) and an important microswitch of receptor activation (Vanni et al., 2010). This configuration resembled those in the initial crystal structure (PDB: 4DKL) and *apo* μOR (Figure 4), so did ICL1 and H8 (Figures 5A–5C). The partial biased agonist buprenorphine showed an in-between behavior. In the CR and the N$^{7.49}$P$^{7.50}$xxY$^{7.53}$-G$^{1.49}$N$^{1.50}$ motifs, buprenorphine

wait, it was well documented?
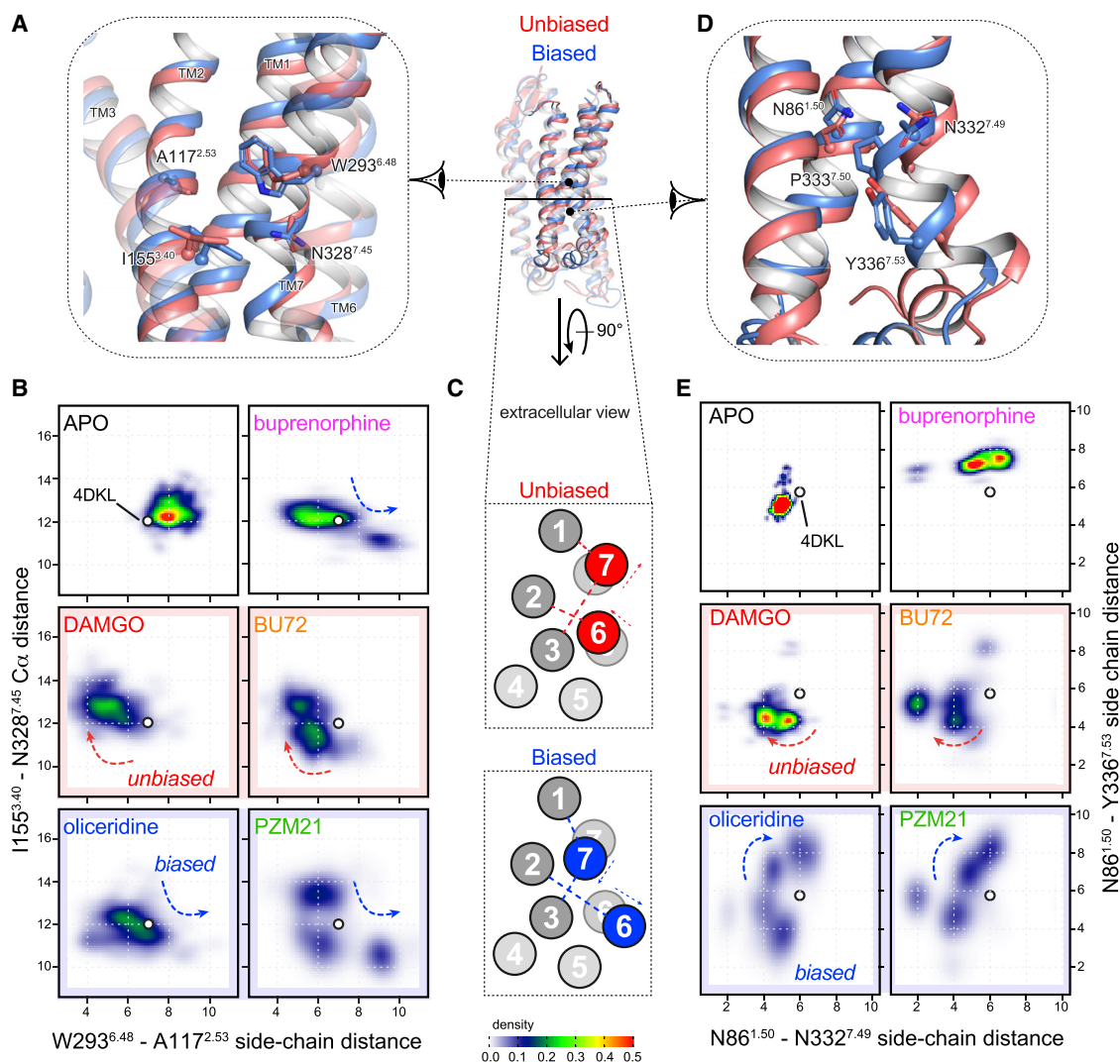
Figure 4. Biased agonists induced conformational changes in the CR and the lower half of TM7

(A and B) In the CR, biased agonist binding (blue) splits the side chains of W293$^{6.48}$ and A117$^{2.53}$, which allows TM7 to approach TM3 (A). The movements are measured by (B) the minimum side-chain distances between W293$^{6.48}$ and A117$^{2.53}$, against the Cα distances between I155$^{3.40}$ and N328$^{7.45}$.

(C) Schematic presentation of the inter-helical movements. Arrows indicate the direction of the movements and dashed lines indicates the distances measured for (B) and (E).

(D and E) In the lower half of TM7, the N$^{7.49}$P$^{7.50}$xxY$^{7.53}$ motif moves away from the G$^{1.49}$N$^{1.50}$ motif in TM1 only for biased agonists (D). This is measured by (E) the side-chain distances between N86$^{1.50}$, N332$^{7.49}$, and Y336$^{7.53}$.

showed similar but weaker impacts than oliceridine and PZM21 (Figures 4B and 4E). The impacts barely reached the ICL1/H8 domains in the simulation timescale (Figures 5A–5C).

The NMR spectra in the ICL1/H8 domain confirmed the above findings. DAMGO, BU72, and buprenorphine binding results in the small loss of signal intensity of these sensors in H8/ICL1 (Figure 5D). Upon binding the biased agonists oliceridine and PZM21, the lysine sensors K98^{ICL1} and K344$^{8.50}$ showed multiple peaks with change in signal intensity, indicating a much more complex conformational equilibrium (Figure 5D). This suggests that the local conformations became more dynamic. Binding of Nb33 led to signal intensity decrease for all the ligands (Figures

S5Q and S7A). We performed REST2-MD simulations on the five receptor-agonist-Nb33 complexes and found similar patterns at ICL1 and H8 (Figure S7B). The distinct conformations associated with oliceridine and PZM21 were still evident in the presence of Nb33 but less remarkable. Nb33 inserts slightly between ICL1 and H8. Thus, it increased the ICL1-H8 distances in all the five complexes, while in the case of oliceridine and PZM21, it also reduced the conformational dynamics in this domain.

Overall, the results suggest that the biased agonists act on the toggle switch W293$^{6.48}$ to trigger conformational changes in TM7, ICL1, and H8 in the ICD. This occurs in an allosteric manner, via the conserved motifs N$^{7.49}$P$^{7.50}$xxY$^{7.53}$ and
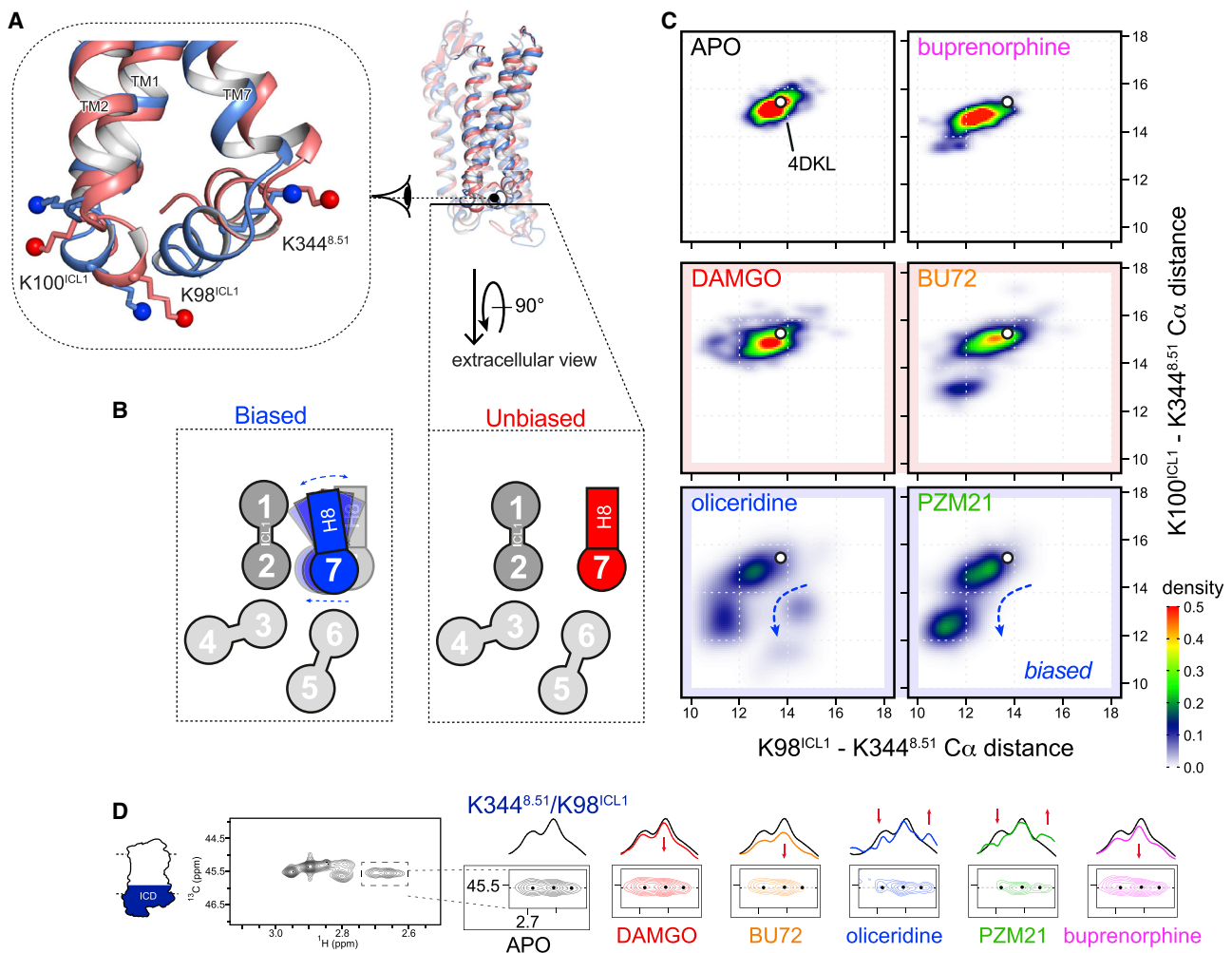
Figure 5. Biased agonists induced new clusters of μOR conformations in ICL1 and H8

(A) Biased agonist binding (blue) triggered inward movements of TM7-H8 toward TM3 and ICL1, respectively, closing the ICL1-H8 cleft.

(B and C) Schematic presentation (B) of the movements in (A) from the extracellular view, as measured by (C) the Cα distances between the NMR sensors K98^{ICL1}, K100^{ICL1}, and K344$^{8.51}$. Density maps of the measured distances illustrate a new cluster of conformations associated with the biased agonists oliceridine and PZM21.

(D) Extracted HMQC spectra of K344$^{8.51}$/K98^{ICL1} resonances of μOR in *apo* form (black) and at saturating concentrations of DAMGO (red), BU72 (orange), oliceridine (blue), PZM21 (green), and buprenorphine (magenta). Dashed black lines indicate the position of the cross-sections shown above the spectra. Black dots indicate the peak centers in *apo* μOR. Red arrows indicate the changes upon agonist binding.

G$^{1.49}$N$^{1.50}$. The conformational changes persist even when the receptor is coupled to Nb33. Although the binding sites of G proteins and arrestins largely overlap, only arrestins interact with ICL1/H8 in the structures of arrestin in complex with rhodopsin, neurotensin receptor 1, β1AR, and M$_2$R (Huang et al., 2020; Lee et al., 2020; Staus et al., 2020; Yin et al., 2019). Therefore, the distinct TM7-ICL1-H8 conformations generated by the biased agonists likely inhibit the binding of β-arrestins but not the G proteins (Figure 6).

DISCUSSION

The pharmacological outcome of a ligand varies with the test systems and conditions, which has led to contradictory findings

and the ongoing debate on whether μOR functional selectivity can separate analgesia from opioid side effects. Even the characterization of functional selectivity itself is debated, because of the lack of deep understanding and field standards. In this study, we provide the basic molecular mechanism of biased and partial agonism in μOR, which is intrinsic to the receptor-ligand interactions and should be consistent under different test conditions. The approach and findings can serve as high-resolution monitors for the design and evaluation of μOR ligands with specific functions (e.g., partial or biased agonism/antagonism/inverse agonism for a specific signaling pathway). Such ligands may serve to pinpoint specific aspects of the μOR signaling network, helping resolve the ongoing debates from bottom up. GPCR ligand design is challenging despite the growing number of
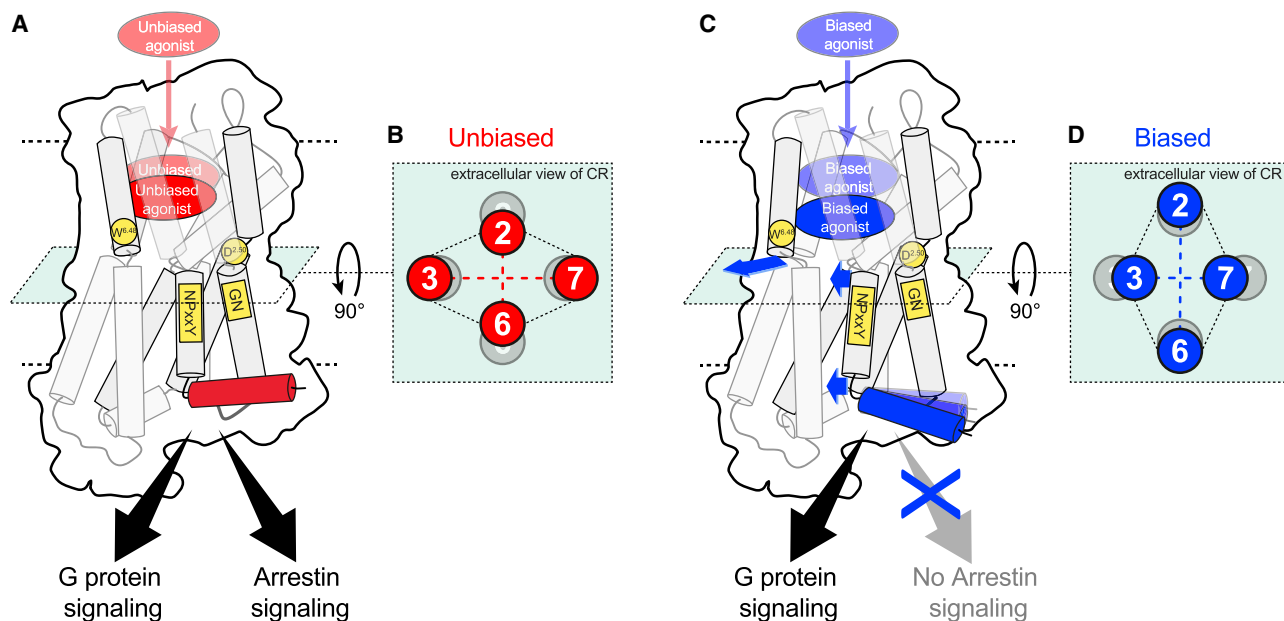
Figure 6. Scheme of the proposed allosteric mechanism of μOR functional selectivity

(A and B) Binding of the unbiased agonists (A) causes W293[6.48] in TM6 to approach TM2 in (B) the connector region.

(C and D) Biased agonists bind deeper in the pocket (C) and separate TM6 from TM2 in (D) the connector region, letting TM7 to approach TM3. This disrupts the interactions between the NPxxY motif, D114[2.50] and the GN motif (C). The lower half of TM7 moves toward TM3, closing the cleft between H8 and ICL1, which may inhibit arrestin signaling (C). Blue arrows indicate the movements associated with allosteric functional selectivity. Conserved residues/motifs involved are highlighted in yellow. The transmembrane helices are represented by two adjoining cylinders colored in gray. The top cylinder of TM1 and TM7 are transparent for clarity.

high-resolution structures. Although structure-based design and screening have lifted the hit rate, tools to design or predict biased ligands are lacking. REST2-MD can identify biased μOR agonists and thus be used for ligand screening. Although it is more costly than docking or standard MD, it provides mechanistic and dynamics insights into the ligand actions, which is essential for the subsequent ligand optimization.

This study highlights the dynamic and allosteric details of μOR pre-activation upon agonist binding, prior to the coupling of intracellular signaling partners. The pre-activation stage is crucial for drug design because it is dictated by the ligands. Nevertheless, it is highly dynamic and inaccessible to X-ray crystallography or cryo-EM. We took advantage of 2D HMQC NMR and enhanced-sampling MD to capture conformational dynamic patterns during the pre-activation, which differentiate the partial and the biased agonists from the full unbiased ones. The phenomenon that biased or partial ligands stabilize distinct receptor conformations has been reported for the angiotensin II receptor 1 (during pre-activation) (Wingler et al., 2019), the glucagon-like peptide-1 receptor (in fully active state) (Liang et al., 2018), the β1AR (Moukhametzianov et al., 2011; Solt et al., 2017), the A$_{2A}$R (Huang et al., 2021; Sušac et al., 2018; Ye et al., 2016) and the β2AR, either in pre-active state (biased agonism) (Liu et al., 2012) or fully active state (partial and biased agonism) (Masureel et al., 2018). Interestingly, Sušac et al. (2018) also found different inward/outward movements of TM7 on the intracellular side upon agonist and antagonist binding, which is consistent with available A$_{2A}$R crystal structures. However, it is unclear

whether the TM7 movements of A$_{2A}$R were associated with ligand bias. One drawback of REST2-MD is the loss of temporal information. Nevertheless, it has been shown that biased agonism in μOR is not controlled by binding or signaling kinetics, suggesting a mechanism dictated by receptor conformations (Pedersen et al., 2020)

Most of the findings here are independent of Nb33, except for the interplay observed between the agonists and Nb33 (between the LBD and the ICD), the mechanism of which remains obscure. The process of G protein binding likely determines the G protein subtype selectivity through transient GPCR-G protein interactions or intermediate conformations (Du et al., 2019; Liu et al., 2019b), but this is beyond the scope of the present study. Without Nb33 or G proteins, however, our NMR and REST2-MD results coherently and robustly illustrated the specific conformational dynamics underlying the partial and biased agonisms. The mechanism relies on highly conserved amino-acid motifs, which may be common for other class A GPCRs.

Limitations of the study

The present study was focused mainly on the inherent mechanism of μOR ligand bias, prior to G protein or arrestin binding. One important question is how G proteins or arrestins respond to the distinct μOR conformations associated with the biased agonists. However, investigations on this aspect have been very challenging technically for both MD and NMR. The size of GPCR-agonist-G protein/arrestin ternary complexes are the major limit. Their conformational changes take place in timescales

This whole paragraph is just too confusing because I have no idea what info am I supposed to get out of these different structures.

that challenge today's all-atom MD simulations. Few high-resolution structures are available, especially for complexes with arrestins. Such ternary complexes are also unstable under NMR experimental conditions because of the destabilizing effect of the detergents. Therefore, studies in this aspect have been limited to G protein or arrestin surrogates (e.g., modified Gα subunits and nanobodies). The aspect of G protein/arrestin binding thus remains to be further explored.

STAR★METHODS

Detailed methods are provided in the online version of this paper and include the following:

- KEY RESOURCES TABLE
- RESOURCE AVAILABILITY
  - Lead contact
  - Materials availability
  - Data and code availability
- EXPERIMENTAL MODEL AND SUBJECT DETAILS
  - Bacterial cells
  - Insect cells
  - Cell lines and transfection
- METHOD DETAILS
  - Cell transfection
  - G protein activation assay
  - GRK2 and GRK5 recruitment assay
  - β-arrestins recruitment assay
  - Internalization assay
  - Fluorescent ligand-binding assay on living cells
  - Membrane preparation and SNAP labeling
  - Fluorescent ligand-binding assay on solubilized receptors
  - (Met-ε)-[$^{13}CH_3$]-μOR-2x M72T expression
  - (Met-ε)-[$^{13}CH_3$]-μOR-2x M72T purification
  - (Met-ε)-[$^{13}CH_3$]-μOR-2x M72T assignment procedure
  - (Met-ε)-[$^{13}CH_3$]-μOR-2x M72T reductive methylation
  - Nanobody Nb33 expression and purification
  - NMR spectroscopy
  - Molecular dynamics simulations
- QUANTIFICATION AND STATISTICAL ANALYSIS

SUPPLEMENTAL INFORMATION

Supplemental information can be found online at https://doi.org/10.1016/j.molcel.2021.07.033.

REFERENCES

Casiraghi, M., Damian, M., Lescop, E., Point, E., Moncoq, K., Morellet, N., Levy, D., Marie, J., Guittet, E., Banères, J.L., and Catoire, L.J. (2016). Functional modulation of a G protein-coupled receptor conformational landscape in a lipid bilayer. J. Am. Chem. Soc. 138, 11170–11175.

Clark, L.D., Dikiy, I., Chapman, K., Rödström, K.E., Aramini, J., LeVine, M.V., Khelashvili, G., Rasmussen, S.G., Gardner, K.H., and Rosenbaum, D.M. (2017). Ligand modulation of sidechain dynamics in a wild-type human GPCR. eLife 6, e28505.

Cong, X., and Golebiowski, J. (2018). Allosteric Na(+)-binding site modulates CXCR4 activation. Physical chemistry chemical physics. Phys. Chem. Chem. Phys. 20, 24915–24920.

Cong, X., Fiorucci, S., and Golebiowski, J. (2018). Activation dynamics of the neurotensin G protein-coupled receptor 1. J. Chem. Theory Comput. 14, 4467–4473.

Cong, X., Cheron, J.B., Golebiowski, J., Antonczak, S., and Fiorucci, S. (2019). Allosteric modulation mechanism of the mGluR5 transmembrane domain. J. Chem. Inf. Model. 59, 2871–2878.

Conibear, A.E., and Kelly, E. (2019). A biased view of μ-opioid receptors? Mol. Pharmacol. 96, 542–549.

Cowan, A., Doxey, J.C., and Harry, E.J. (1977a). The animal pharmacology of buprenorphine, an oripavine analgesic agent. Br. J. Pharmacol. 60, 547–554.

Cowan, A., Lewis, J.W., and Macfarlane, I.R. (1977b). Agonist and antagonist properties of buprenorphine, a new antinociceptive agent. Br. J. Pharmacol. 60, 537–545.

Delaglio, F., Grzesiek, S., Vuister, G.W., Zhu, G., Pfeifer, J., and Bax, A. (1995). NMRPipe: a multidimensional spectral processing system based on UNIX pipes. J. Biomol. NMR 6, 277–293.

DeWire, S.M., Yamashita, D.S., Rominger, D.H., Liu, G., Cowan, C.L., Graczyk, T.M., Chen, X.T., Pitis, P.M., Gotchev, D., Yuan, C., et al. (2013). A G protein-biased ligand at the μ-opioid receptor is potently analgesic with reduced gastrointestinal and respiratory dysfunction compared with morphine. J. Pharmacol. Exp. Ther. 344, 708–717.

Dickson, C.J., Madej, B.D., Skjevik, A.A., Betz, R.M., Teigen, K., Gould, I.R., and Walker, R.C. (2014). Lipid14: the amber lipid force field. J. Chem. Theory Comput. 10, 865–879.

Dror, R.O., Arlow, D.H., Maragakis, P., Mildorf, T.J., Pan, A.C., Xu, H., Borhani, D.W., and Shaw, D.E. (2011). Activation mechanism of the β2-adrenergic receptor. Proc. Natl. Acad. Sci. U S A 108, 18684–18689.

Du, Y., Duc, N.M., Rasmussen, S.G.F., Hilger, D., Kubiak, X., Wang, L., Bohon, J., Kim, H.R., Wegrecki, M., Asuru, A., et al. (2019). Assembly of a GPCR-G protein complex. Cell 177, 1232–1242.e11.

Eddy, M.T., Lee, M.Y., Gao, Z.G., White, K.L., Didenko, T., Horst, R., Audet, M., Stanczak, P., McClary, K.M., Han, G.W., et al. (2018). Allosteric coupling of drug binding and intracellular signaling in the A$_{2A}$ adenosine receptor. Cell 172, 68–80.e12.

Ehrlich, A.T., Semache, M., Gross, F., Da Fonte, D.F., Runtz, L., Colley, C., Mezni, A., Le Gouill, C., Lukasheva, V., Hogue, M., et al. (2019). Biased signaling of the mu opioid receptor revealed in native neurons. iScience 14, 47–57.

Emmerson, P.J., Liu, M.R., Woods, J.H., and Medzihradsky, F. (1994). Binding affinity and selectivity of opioids at mu, delta and kappa receptors in monkey brain membranes. J. Pharmacol. Exp. Ther. 271, 1630–1637.

Frisch, M.J., Trucks, G.W., Schlegel, H.B., Scuseria, G.E., Robb, M.A., Cheeseman, J.R., Scalmani, G., Barone, V., Mennucci, B., Petersson, G.A., et al. (2009). Gaussian 09, revision A.02 (Wallingford, CT: Gaussian).

Gillis, A., Gondin, A.B., Kliewer, A., Sanchez, J., Lim, H.D., Alamein, C., Manandhar, P., Santiago, M., Fritzwanker, S., Schmiedel, F., et al. (2020). Low intrinsic efficacy for G protein activation can explain the improved side effect profiles of new opioid agonists. Sci. Signal. 13, eaaz3140.

Gordon, J.C., Myers, J.B., Folta, T., Shoja, V., Heath, L.S., and Onufriev, A. (2005). H++: a server for estimating pKas and adding missing hydrogens to macromolecules. Nucleic Acids Res. 33, W368–W371.

Handa, B.K., Land, A.C., Lord, J.A., Morgan, B.A., Rance, M.J., and Smith, C.F. (1981). Analogues of beta-LPH61-64 possessing selective agonist activity at mu-opiate receptors. Eur. J. Pharmacol. 70, 531–540.

Hill, R., Disney, A., Conibear, A., Sutcliffe, K., Dewey, W., Husbands, S., Bailey, C., Kelly, E., and Henderson, G. (2018). The novel μ-opioid receptor agonist PZM21 depresses respiration and induces tolerance to antinociception. Br. J. Pharmacol. 175, 2653–2661.

Huang, W., Manglik, A., Venkatakrishnan, A.J., Laeremans, T., Feinberg, E.N., Sanborn, A.L., Kato, H.E., Livingston, K.E., Thorsen, T.S., Kling, R.C., et al. (2015). Structural insights into μ-opioid receptor activation. Nature 524, 315–321.

Huang, W., Masureel, M., Qu, Q., Janetzko, J., Inoue, A., Kato, H.E., Robertson, M.J., Nguyen, K.C., Glenn, J.S., Skiniotis, G., and Kobilka, B.K. (2020). Structure of the neurotensin receptor 1 in complex with β-arrestin 1. Nature 579, 303–308.

Huang, S.K., Pandey, A., Tran, D.P., Villanueva, N.L., Kitao, A., Sunahara, R.K., Sljoka, A., and Prosser, R.S. (2021). Delineating the conformational landscape of the adenosine A2A receptor during G protein coupling. Cell 184, 1884–1894.e14.

Hulme, E.C., and Trevethick, M.A. (2010). Ligand binding assays at equilibrium: validation and interpretation. Br. J. Pharmacol. 161, 1219–1237.

Isogai, S., Deupi, X., Opitz, C., Heydenreich, F.M., Tsai, C.J., Brueckner, F., Schertler, G.F., Veprintsev, D.B., and Grzesiek, S. (2016). Backbone NMR reveals allosteric signal transduction networks in the β1-adrenergic receptor. Nature 530, 237–241.

Jorgensen, W.L., Chandrasekhar, J., Madura, J.D., Impey, R.W., and Klein, M.L. (1983). Comparison of simple potential functions for simulating liquid water. J. Chem. Phys. 79, 926–935.

Joung, I.S., and Cheatham, T.E., 3rd (2008). Determination of alkali and halide monovalent ion parameters for use in explicitly solvated biomolecular simulations. J. Phys. Chem. B 112, 9020–9041.

Katritch, V., Fenalti, G., Abola, E.E., Roth, B.L., Cherezov, V., and Stevens, R.C. (2014). Allosteric sodium in class A GPCR signaling. Trends Biochem. Sci. 39, 233–244.

Kelly, E. (2013). Efficacy and ligand bias at the μ-opioid receptor. Br. J. Pharmacol. 169, 1430–1446.

Kliewer, A., Schmiedel, F., Sianati, S., Bailey, A., Bateman, J.T., Levitt, E.S., Williams, J.T., Christie, M.J., and Schulz, S. (2019). Phosphorylation-deficient G-protein-biased μ-opioid receptors improve analgesia and diminish tolerance but worsen opioid side effects. Nat. Commun. 10, 367.

Kliewer, A., Gillis, A., Hill, R., Schmiedel, F., Bailey, C., Kelly, E., Henderson, G., Christie, M.J., and Schulz, S. (2020). Morphine-induced respiratory depression is independent of β-arrestin2 signalling. Br. J. Pharmacol. 177, 2923–2931.

Koehl, A., Hu, H., Maeda, S., Zhang, Y., Qu, Q., Paggi, J.M., Latorraca, N.R., Hilger, D., Dawson, R., Matile, H., et al. (2018). Structure of the μ-opioid receptor-Gi protein complex. Nature 558, 547–552.

Kofuku, Y., Ueda, T., Okude, J., Shiraishi, Y., Kondo, K., Mizumura, T., Suzuki, S., and Shimada, I. (2014). Functional dynamics of deuterated β2 -adrenergic receptor in lipid bilayers revealed by NMR spectroscopy. Angew. Chem. Int. Ed. Engl. 53, 13376–13379.

Kohlhoff, K.J., Shukla, D., Lawrenz, M., Bowman, G.R., Konerding, D.E., Belov, D., Altman, R.B., and Pande, V.S. (2014). Cloud-based simulations on Google Exacycle reveal ligand modulation of GPCR activation pathways. Nat. Chem. 6, 15–21.

Latorraca, N.R., Venkatakrishnan, A.J., and Dror, R.O. (2017). GPCR dynamics: structures in motion. Chem. Rev. 117, 139–155.

Lee, Y., Warne, T., Nehmé, R., Pandey, S., Dwivedi-Agnihotri, H., Chaturvedi, M., Edwards, P.C., García-Nafría, J., Leslie, A.G.W., Shukla, A.K., and Tate, C.G. (2020). Molecular basis of β-arrestin coupling to formoterol-bound β1-adrenoceptor. Nature 583, 862–866.

Liang, Y.L., Khoshouei, M., Glukhova, A., Furness, S.G.B., Zhao, P., Clydesdale, L., Koole, C., Truong, T.T., Thal, D.M., Lei, S., et al. (2018). Phase-plate cryo-EM structure of a biased agonist-bound human GLP-1 receptor-Gs complex. Nature 555, 121–125.

Lindorff-Larsen, K., Piana, S., Palmo, K., Maragakis, P., Klepeis, J.L., Dror, R.O., and Shaw, D.E. (2010). Improved side-chain torsion potentials for the Amber ff99SB protein force field. Proteins 78, 1950–1958.

Liu, J.J., Horst, R., Katritch, V., Stevens, R.C., and Wüthrich, K. (2012). Biased signaling pathways in β2-adrenergic receptor characterized by 19F-NMR. Science 335, 1106–1110.

Liu, X., Ahn, S., Kahsai, A.W., Meng, K.C., Latorraca, N.R., Pani, B., Venkatakrishnan, A.J., Masoudi, A., Weis, W.I., Dror, R.O., et al. (2017). Mechanism of intracellular allosteric β2AR antagonist revealed by X-ray crystal structure. Nature 548, 480–484.

Liu, X., Masoudi, A., Kahsai, A.W., Huang, L.Y., Pani, B., Staus, D.P., Shim, P.J., Hirata, K., Simhal, R.K., Schwalb, A.M., et al. (2019a). Mechanism of β2AR regulation by an intracellular positive allosteric modulator. Science 364, 1283–1287.

Liu, X., Xu, X., Hilger, D., Aschauer, P., Tiemann, J.K.S., Du, Y., Liu, H., Hirata, K., Sun, X., Guixà-González, R., et al. (2019b). Structural insights into the process of GPCR-G protein complex formation. Cell 177, 1243–1251.e12.

Lovera, S., Cuzzolin, A., Kelm, S., De Fabritiis, G., and Sands, Z.A. (2019). Reconstruction of apo A2A receptor activation pathways reveal ligand-competent intermediates and state-dependent cholesterol hotspots. Sci. Rep. 9, 14199.

Manglik, A., Kruse, A.C., Kobilka, T.S., Thian, F.S., Mathiesen, J.M., Sunahara, R.K., Pardo, L., Weis, W.I., Kobilka, B.K., and Granier, S. (2012). Crystal structure of the μ-opioid receptor bound to a morphinan antagonist. Nature 485, 321–326.

Manglik, A., Kim, T.H., Masureel, M., Altenbach, C., Yang, Z., Hilger, D., Lerch, M.T., Kobilka, T.S., Thian, F.S., Hubbell, W.L., et al. (2015). Structural insights into the dynamic process of β2-adrenergic receptor signaling. Cell 161, 1101–1111.

Manglik, A., Lin, H., Aryal, D.K., McCorvy, J.D., Dengler, D., Corder, G., Levit, A., Kling, R.C., Bernat, V., Hübner, H., et al. (2016). Structure-based discovery of opioid analgesics with reduced side effects. Nature 537, 185–190.

Masureel, M., Zou, Y., Picard, L.P., van der Westhuizen, E., Mahoney, J.P., Rodrigues, J.P.G.L.M., Mildorf, T.J., Dror, R.O., Shaw, D.E., Bouvier, M., et al. (2018). Structural insights into binding specificity, efficacy and bias of a β2AR partial agonist. Nat. Chem. Biol. 14, 1059–1066.

McPherson, J., Rivero, G., Baptist, M., Llorente, J., Al-Sabah, S., Krasel, C., Dewey, W.L., Bailey, C.P., Rosethorne, E.M., Charlton, S.J., et al. (2010). μ-opioid receptors: correlation of agonist efficacy for signalling with ability to activate internalization. Mol. Pharmacol. 78, 756–766.

Miao, Y., Nichols, S.E., Gasper, P.M., Metzger, V.T., and McCammon, J.A. (2013). Activation and dynamic network of the M2 muscarinic receptor. Proc. Natl. Acad. Sci. U S A 110, 10982–10987.

Moukhametzianov, R., Warne, T., Edwards, P.C., Serrano-Vega, M.J., Leslie, A.G., Tate, C.G., and Schertler, G.F. (2011). Two distinct conformations of helix

6 observed in antagonist-bound structures of a beta1-adrenergic receptor. Proc. Natl. Acad. Sci. U S A *108*, 8228–8232.

Neilan, C.L., Husbands, S.M., Breeden, S., Ko, M.C., Aceto, M.D., Lewis, J.W., Woods, J.H., and Traynor, J.R. (2004). Characterization of the complex morphinan derivative BU72 as a high efficacy, long-lasting mu-opioid receptor agonist. Eur. J. Pharmacol. *499*, 107–116.

Nygaard, R., Zou, Y., Dror, R.O., Mildorf, T.J., Arlow, D.H., Manglik, A., Pan, A.C., Liu, C.W., Fung, J.J., Bokoch, M.P., et al. (2013). The dynamic process of β(2)-adrenergic receptor activation. Cell *152*, 532–542.

Okude, J., Ueda, T., Kofuku, Y., Sato, M., Nobuyama, N., Kondo, K., Shiraishi, Y., Mizumura, T., Onishi, K., Natsume, M., et al. (2015). Identification of a conformational equilibrium that determines the efficacy and functional selectivity of the μ-opioid receptor. Angew. Chem. Int. Ed. Engl. *54*, 15771–15776.

Patriksson, A., and van der Spoel, D. (2008). A temperature predictor for parallel tempering simulations. Phys. Chem. Chem. Phys. *10*, 2073–2077.

Pedersen, M.F., Wróbel, T.M., Märcher-Rørsted, E., Pedersen, D.S., Møller, T.C., Gabriele, F., Pedersen, H., Matosiuk, D., Foster, S.R., Bouvier, M., and Bräuner-Osborne, H. (2020). Biased agonism of clinically approved μ-opioid receptor agonists and TRV130 is not controlled by binding and signaling kinetics. Neuropharmacology *166*, 107718.

Raehal, K.M., Schmid, C.L., Groer, C.E., and Bohn, L.M. (2011). Functional selectivity at the μ-opioid receptor: implications for understanding opioid analgesia and tolerance. Pharmacol. Rev. *63*, 1001–1019.

Schmid, C.L., Kennedy, N.M., Ross, N.C., Lovell, K.M., Yue, Z., Morgenweck, J., Cameron, M.D., Bannister, T.D., and Bohn, L.M. (2017). Bias factor and therapeutic window correlate to predict safer opioid analgesics. Cell *171*, 1165–1175.e13.

Schott-Verdugo, S., and Gohlke, H. (2019). PACKMOL-Memgen: a simple-to-use, generalized workflow for membrane-protein-lipid-bilayer system building. J. Chem. Inf. Model. *59*, 2522–2528.

Sena, D.M., Jr., Cong, X., Giorgetti, A., Kless, A., and Carloni, P. (2017). Structural heterogeneity of the μ-opioid receptor's conformational ensemble in the apo state. Sci. Rep. *8*, 45761.

Shimada, I., Ueda, T., Kofuku, Y., Eddy, M.T., and Wüthrich, K. (2019). GPCR drug discovery: integrating solution NMR data with crystal and cryo-EM structures. Nat. Rev. Drug Discov. *18*, 59–82.

Solt, A.S., Bostock, M.J., Shrestha, B., Kumar, P., Warne, T., Tate, C.G., and Nietlispach, D. (2017). Insight into partial agonism by observing multiple equilibria for ligand-bound and G$_s$-mimetic nanobody-bound β$_1$-adrenergic receptor. Nat. Commun. *8*, 1795.

Sounier, R., Mas, C., Steyaert, J., Laeremans, T., Manglik, A., Huang, W., Kobilka, B.K., Déméné, H., and Granier, S. (2015). Propagation of conformational changes during μ-opioid receptor activation. Nature *524*, 375–378.

Sounier, R., Yang, Y., Hagelberger, J., Granier, S., and Déméné, H. (2017). ^{1}H, ^{13}C and ^{15}N backbone chemical shift assignments of camelid single-domain antibodies against active state μ-opioid receptor. Biomol. NMR Assign. *11*, 117–121.

Staus, D.P., Hu, H., Robertson, M.J., Kleinhenz, A.L.W., Wingler, L.M., Capel, W.D., Latorraca, N.R., Lefkowitz, R.J., and Skiniotis, G. (2020). Structure of the M2 muscarinic receptor-β-arrestin complex in a lipid nanodisc. Nature *579*, 297–302.

Sušac, L., Eddy, M.T., Didenko, T., Stevens, R.C., and Wüthrich, K. (2018). A$_{2A}$ adenosine receptor functional states characterized by ^{19}F-NMR. Proc. Natl. Acad. Sci. U S A *115*, 12733–12738.

Traynor, J.R., and Nahorski, S.R. (1995). Modulation by mu-opioid agonists of guanosine-5′-O-(3-[35S]thio)triphosphate binding to membranes from human neuroblastoma SH-SY5Y cells. Mol. Pharmacol. *47*, 848–854.

Tribello, G.A., Bonomi, M., Branduardi, D., Camilloni, C., and Bussi, G. (2014). PLUMED 2: new feathers for an old bird. Comput. Phys. Commun. *185*, 604–613.

Trott, O., and Olson, A.J. (2010). AutoDock Vina: improving the speed and accuracy of docking with a new scoring function, efficient optimization, and multithreading. J. Comput. Chem. *31*, 455–461.

Van Der Spoel, D., Lindahl, E., Hess, B., Groenhof, G., Mark, A.E., and Berendsen, H.J. (2005). GROMACS: fast, flexible, and free. J. Comput. Chem. *26*, 1701–1718.

Vanni, S., Neri, M., Tavernelli, I., and Rothlisberger, U. (2010). A conserved protonation-induced switch can trigger "ionic-lock" formation in adrenergic receptors. J. Mol. Biol. *397*, 1339–1349.

Vranken, W.F., Boucher, W., Stevens, T.J., Fogh, R.H., Pajon, A., Llinas, M., Ulrich, E.L., Markley, J.L., Ionides, J., and Laue, E.D. (2005). The CCPN data model for NMR spectroscopy: development of a software pipeline. Proteins *59*, 687–696.

Wang, J.M., Cieplak, P., and Kollman, P.A. (2000). How well does a restrained electrostatic potential (RESP) model perform in calculating conformational energies of organic and biological molecules? J. Comput. Chem. *21*, 1049–1074.

Wang, J., Wolf, R.M., Caldwell, J.W., Kollman, P.A., and Case, D.A. (2004). Development and testing of a general amber force field. J. Comput. Chem. *25*, 1157–1174.

Wang, L., Friesner, R.A., and Berne, B.J. (2011). Replica exchange with solute scaling: a more efficient version of replica exchange with solute tempering (REST2). J. Phys. Chem. B *115*, 9431–9438.

Weis, W.I., and Kobilka, B.K. (2018). The molecular basis of G protein-coupled receptor activation. Annu. Rev. Biochem. *87*, 897–919.

Wingler, L.M., Elgeti, M., Hilger, D., Latorraca, N.R., Lerch, M.T., Staus, D.P., Dror, R.O., Kobilka, B.K., Hubbell, W.L., and Lefkowitz, R.J. (2019). Angiotensin analogs with divergent bias stabilize distinct receptor conformations. Cell *176*, 468–478.e11.

Xu, J., Hu, Y., Kaindl, J., Risel, P., Hübner, H., Maeda, S., Niu, X., Li, H., Gmeiner, P., Jin, C., and Kobilka, B.K. (2019). Conformational complexity and dynamics in a muscarinic receptor revealed by NMR spectroscopy. Mol. Cell *75*, 53–65.e7.

Ye, L., Van Eps, N., Zimmer, M., Ernst, O.P., and Prosser, R.S. (2016). Activation of the A2A adenosine G-protein-coupled receptor by conformational selection. Nature *533*, 265–268.

Yin, W., Li, Z., Jin, M., Yin, Y.L., de Waal, P.W., Pal, K., Yin, Y., Gao, X., He, Y., Gao, J., et al. (2019). A complex structure of arrestin-2 bound to a G protein-coupled receptor. Cell Res. *29*, 971–983.

Yuan, S., Palczewski, K., Peng, Q., Kolinski, M., Vogel, H., and Filipek, S. (2015). The mechanism of ligand-induced activation or inhibition of μ- and κ-opioid receptors. Angew. Chem. Int. Ed. Engl. *54*, 7560–7563.

Yudin, Y., and Rohacs, T. (2019). The G-protein-biased agents PZM21 and TRV130 are partial agonists of μ-opioid receptor-mediated signalling to ion channels. Br. J. Pharmacol. *176*, 3110–3125.

STAR★METHODS

KEY RESOURCES TABLE

REAGENT or RESOURCE	SOURCE	IDENTIFIER
Bacterial and virus strains		
E. coli cells BL21(DE3)	NEB	C2527
E. coli cells DH5α	NEB	C2987
E. coli cells DH10Bac	invitrogen	10361012
Chemicals, peptides, and recombinant proteins		
pFastBac vector	Thermofisher	Cat#10712024
pCDNA3.1 vector	Thermofisher	Cat#V79020
pVL1392 vector	Expression Systems	91-030
Tag-Lite buffer 5x	PerkinElmer/Cisbio	Cat#LABMED
SNAP-Lumi4-Tb	PerkinElmer/Cisbio	Cat#SSNPTBX
SNAP-red	PerkinElmer/Cisbio	Cat#SSNPREDF
Coelenterazine H	invitrogen	Cat#C6780
Naltrexone-d2	PerkinElmer/Cisbio	Cat#L0005RED
Iodoacetamide	Sigma	Cat#I6125
Leupetin	Euromedex	Cat#SP-04-2217
Benzamidine	Sigma	Cat#B6506
Phenylmethanesulfonyl fluoride (PMSF)	Sigma	Cat#P7626
n-dodecyl-beta-D-maltopyranoside (DDM)	Anatrace	Cat#D310
Lauryl maltose neopentyl glycol (LMNG)	Anatrace	Cat#NG310
Cholesterol hemisucinate (CHS)	Sigma	Cat#C6512
Sodium Cholate hydrate	Sigma	Cat#C1254
ANTI-FLAG® M1 Agarose Affinity Gel	Sigma-Aldrich	Cat#A4596
ANTI-FLAG® M2 Agarose Affinity Gel	Sigma-Aldrich	Cat#A2220
FLAG peptide (DYKDDDDK)	Covalab	https://www.covalab.com/peptide-synthesis
Monoclonal ANTI-FLAG® M2 antibody	Sigma-Aldrich	Cat#F3165; RRID:AB_259529
ESF921 culture medium, Methionine Deficient	Expression Systems	Cat#96-200
EX-CELL420 Serum-Free Medium	Sigma-Aldrich	Cat#14420
L-Methionine (methyl-^{13}C, 99%)	Eurisotop	Cat#DLM-206-0
Deuterium oxide (D_2O)	Eurisotop	Cat#D214
2,2-dimethyl-2-silapentane-5-sulfonic acid (DSS)	Eurisotop	Cat#DLM-32
HEPES (D18, 98%)	Eurisotop	Cat#DLM-3786
Dimethyl sulfoxide-d_6	Sigma-Aldrich	Cat#151874
Formaldehyde (^{13}C, 99%) 20 wt.%	Sigma-Aldrich	Cat#489417
Sodium cyanoborohdride ($NaBH_3CN$)	Sigma-Aldrich	Cat#156159
Buprenorphine hydrochloride	Sigma-Aldrich	Cat#B9275
TRV130 hydrochloride	Cliniscience	Cat#HY-16655A
[D-Ala^2, N-Me-Phe^4, Gly^5-ol]-Enkephalin acetate salt (DAMGO)	Sigma-Aldrich	Cat#E7384
BU72	Prof. Peter Gmeiner	N/A
PZM21	Prof. Peter Gmeiner	N/A
Experimental models: Cell lines		
insect cell line Sf9	Life Technologies	Cat#11496015
HEK293 human cells	ATCC	CRL-1573

(Continued on next page)

Continued

REAGENT or RESOURCE	SOURCE	IDENTIFIER
Recombinant DNA		
pVL1392-μOR-2x-M72T	Sounier et al., 2015	N/A
pFastBac-μOR-2x-M72T	Sounier et al., 2015	N/A
pFastBac-μOR-2x-M72T-mutant	This study	N/A
pcDNA-μOR-YFP	This study	N/A
pcDNA-SNAP-μOR	This study	N/A
pcDNA-μOR-2x-M72T	This study	N/A
pcDNA-GRK2-RLuc	ARPEGE	https://www.arpege.cnrs.fr/
pcDNA-FLAG-Gβ2	ARPEGE	https://www.arpege.cnrs.fr/
pcDNA-Gγ1-Venus	ARPEGE	https://www.arpege.cnrs.fr/
pcDNA-Venus-Gγ2	ARPEGE	https://www.arpege.cnrs.fr/
pcDNA-Gαi1-RLuc8	ARPEGE	https://www.arpege.cnrs.fr/
pcDNA-Gαi2-RLuc8	ARPEGE	https://www.arpege.cnrs.fr/
pcDNA-Gαi3-RLuc8	ARPEGE	https://www.arpege.cnrs.fr/
pcDNA-GαOA-RLuc8	ARPEGE	https://www.arpege.cnrs.fr/
pcDNA-GαOB-RLuc8	ARPEGE	https://www.arpege.cnrs.fr/
pcDNA-arrestin1-RLuc	ARPEGE	https://www.arpege.cnrs.fr/
pcDNA-arrestin2-RLuc	ARPEGE	https://www.arpege.cnrs.fr/
pMal-p2x-Nb33	Sounier et al., 2017	https://bmrb.io/data_library/summary/?bmrbId=26936
Software and algorithms		
PyMOL	Schrödinger	https://pymol.org/2/
Prism v.6.0	GraphPad Software	https://www.graphpad.com/scientific-software/prism/
NMRpipe	Delaglio et al., 1995	https://www.ibbr.umd.edu/nmrpipe/install.html
CCPNMR Analysis v3.0	Vranken et al., 2005	https://www.ccpn.ac.uk/v2-software/software/analysis
Autodock Vina	Trott and Olson, 2010	http://vina.scripps.edu/
H++ server	Gordon et al., 2005	http://biophysics.cs.vt.edu/
GROMACS 5.1	Van Der Spoel et al., 2005	https://www.gromacs.org
PLUMED 2.3	Tribello et al., 2014	https://www.plumed.org/
PACKMOL-Memgen	Schott-Verdugo and Gohlke, 2019	https://github.com/alanwilter/acpype/blob/master/amber19-0_linux/bin/packmol-memgen

RESOURCE AVAILABILITY

Lead contact
Further information and requests for resources and reagents should be directed to and will be fulfilled by the lead contact, Rémy Sounier (remy.sounier@igf.cnrs.fr).

Materials availability
DNA constructs generated by the authors and from ARPEGE can be obtained upon request from the lead contact, but we may require a payment and/or a completed Materials Transfer Agreement if there is potential for commercial application.

Data and code availability
All data reported in this paper will be shared by the lead contact upon request.

This paper does not report any original codes.

Any additional information required to reproduce this work is available from the lead contact.

EXPERIMENTAL MODEL AND SUBJECT DETAILS

Bacterial cells
E. coli BL21(DE3) were grown in LB at 37°C.

Insect cells
Recombinant baculoviruses were generated using the BestBac or pFastBac baculovirus system according to manufacturer's instructions (Expression Systems, ThermoFischer, respectively). High titer baculoviruses encoding genes were used to infect *Sf*9 cells at a cell density of 4×10^6 cells per ml in suspension in methionine deficient media (Expression System) in the presence of 3 μM naloxone with ^{13}C methyl labeled methionine (Cambridge Isotope) added into the media at 250 mg·L^{-1} concentration. Cells were harvested by centrifugation 48 h post-infection and stored at −80°C until purification.

Cell lines and transfection
HEK293 cells were grown in Dulbecco's Modified Eagle's Medium (DMEM, Life Technologies) supplemented with 10% fetal bovine serum (FBS, Life Technologies) without antibiotics at 37°C, 5% CO_2.

METHOD DETAILS

Cell transfection
Transient transfection was performed using lipofectamine2000 (Invitrogen Life Technologies). Depending on the assay, HEK293 cells were stimulated 24h or 48h after transfection. For G protein activation and GRK2/5 recruitment, cells were seeded into a 6-well plate for 24h at a density of 750,000 cells per well. Cells were then detached, seeded and incubated for 24h in a 96-well white plate coated with poly-$_L$-Ornithine at a density of 40,000 cells per well. For the signaling assays, we used three different constructs of full-length μOR (SNAP-μOR, μOR-2x-M72T, and μOR-YFP) depending on the experiment to be conducted (i.e., TR-FRET, BRET Gi and arrestin recruitment, respectively). For binding, β-arrestins recruitment and internalization assays, cells were directly transfected into a 96-well white plate coated with poly-$_L$-Ornithine at a density of 40,000 cells per well following manufacturer's recommended proto-col. For binding assay on membrane and solubilized receptors cells were transfected using electroporation. Electroporation was per-formed in a volume of 400 μL with a total 5 μg SNAP-μOR plasmid and 20,000,000 cells in electroporation buffer (50 mM K_2HPO_4, 20 mM CH_3COOK, and 20 mM KOH, pH 7.4). After electroporation (260 V, 1 mF, Bio–Rad Gene Pulser electroporator), cells were resuspended in 15 mL DMEM supplemented with 10% FBS in T150 culture dishes (pretreated with Poly-L-Ornithine) for 24 h.

G protein activation assay
The cells were transfected with 4 plasmids encoding the mouse μOR receptor (Flag-μOR-2x), the β2 and Venus-γ2 G protein subunits and the Gα protein fused with a donor at a 1:1:1:1 ratio. Gαi1, Gαi2, Gαi3, GαOA and GαOB was fused to *Renilla Luciferase2* (Rluc8 provided by the ARPEGE platform). 24 h after transfection, cells were washed twice with PBS complemented with 0.9 mM $CaCl_2$ and 0.5 mM $MgCl_2$. Basal conditions were achieved by the addition of PBS solutions, followed by Coelenterazine H at a final concentra-tion of 5 μM. To evaluate the effects of the μOR agonists, the addition of Coelenterazine H was followed by stimulation with different agonists. Activation of the μOR promotes dissociation of the Gαβγ protein complex resulting in the Bioluminescence resonance energy transfer (BRET) signal decay. BRET between Rluc8 and Venus was measured after the addition of the Rluc8 substrate Coelenterazine H. BRET readings were collected using a Mithras LB940 plate reader (Berthold technologies, Rluc8 485 ± 20 nm; YFP 530 ± 25 nm) and the reading chamber was maintained at 37°C throughout the entire reading time. The BRET signal was calcu-lated by the ratio of emission of Venus (535 nm) to Rluc8 (480 nm):

$$mBRET = \left((\text{Ratio } 535/480)_{assay} - (\text{Ratio } 535/480)_{Rluc8\ alone} \right) \times 1000$$

GRK2 and GRK5 recruitment assay
The cells were transfected with 2 plasmids encoding the human μOR receptor fused to YFP at the C-terminal, and GRK2/5 was fused to *Renilla Luciferase2* (provided by the ARPEGE platform). 24 h after transfection, cells were washed twice with PBS complemented with 0.9 mM $CaCl_2$ and 0.5 mM $MgCl_2$. The cells were incubated with Coelenterazine H at a final concentration of 5 μM, followed by stimulation with agonists before the BRET readings were captured. Recruitment of GRK2/5 is assessed by an increase in the BRET signal.

β-arrestins recruitment assay
The cells were transfected with 2 plasmids encoding the human μOR receptor fused to YFP at the C-terminal, and β-arrestin-1/β-arrestin-2 was fused to *Renilla Luciferase1* at the N-terminal (provided by Dr. M. Scott to the ARPEGE platform). 24 h after transfection, cells were washed twice with PBS complemented with 0.9 mM $CaCl_2$ and 0.5 mM $MgCl_2$. The cells were incubated

with Coelenterazine H at a final concentration of 5 μM, followed by stimulation with agonists before the BRET readings were captured. Recruitments of β-arrestin-1 and β-arrestin-2 are assessed by an increase in the BRET signal.

Internalization assay

The cells were transfected with one plasmid encoding the SNAP-μOR receptor. 24 hours after transfection, SNAP-μOR cells were washed with Tag-Lite buffer (PerkinElmer/CisBio Bioassays) and incubated at 37°C with benzylguanine-Lumi4-Tb (SNAP-Lumi4-Tb) at a concentration of 100 nM during 1 hour. The cells were washed 4 times with Tag-Lite buffer and then incubated with μOR agonists diluted in fluorescein buffer (24 μM). Reading was performed at 37°C on an Infinite F500® plate reader (TECAN, Lumi4-Terbium-criptate: 620 ± 10 nm; Fluorescein: 520 ± 10 nm) with an excitation at 337 nm and emission at 620 nm and 520 nm. Receptor internalization was monitored by time-resolved fluorescent resonance energy transfer (TR-FRET) at 37 °C during 70–80 min. The signal was calculated by the ratio of emission of terbium cryptate (620 nm) to fluorescein (520 nm): $\Delta R = (Ratio\ 620/520) \times 10,000$.

Fluorescent ligand-binding assay on living cells

HEK293 cells transfected with SNAP-μOR plasmid were seeded at a density of 40,000 cells per well in 96-well white plates coated with poly-L-Ornithine. 24h after transfection, SNAP-μOR was labeled 1 h at 37°C with 100nM SNAP-Lumi4-Tb diluted in Tag-lite labeling buffer. Fluorescent naltrexone and agonists were diluted in Tag-lite labeling buffer. A fixed concentration of fluorescent naltrexone-d2 was determined (0.5 nM = K_d) and used. Increasing concentration of agonists was added prior to the addition of fluorescent naltrexone-d2 in the plates containing labeled cells. Plates were incubated overnight at 4°C before homogeneous time-resolved Fluorescent (HTRF) signal detection. HTRF detection was performed on a PHERAstar (BMG labtechnologies). The signal was collected both at 665 nm and 620 nm. HTRF ratio was obtained by dividing the acceptor signal at 665 nm by the donor signal at 620 nm and multiplying this value by 10,000.

Membrane preparation and SNAP labeling

Twenty-four hours after transfection cells were washed once with PBS solution, scraped and then collected by centrifugation 5 minutes at 300 g. The cell pellet was resuspended in 20 mL lysis buffer (10 mM HEPES, 1 mM EDTA) and homogenized using an electric homogenizer on ice. After centrifugation 5 min at 1,000 g at 4°C, the pellet was discarded and the supernatant was centrifuged at 30,000 g for 30 min at 4°C. The resulting pellet was resuspended in 2 mL of Tag-Lite buffer containing 300 nM BG-Lumi4-Tb and incubated for 1 hour at 4°C under circle rotator. Membranes were then resuspensed in 2 mL PBS to remove the excess of BG-Lumi4-Tb and centrifuged at 30,000 g for 30 min on a bentchtop centrifuge. This step was reproduced twice. Protein concentration was determined by BCA using BSA as standard. SNAP-μOR membranes were aliquoted and stored at −80°C.

Fluorescent ligand-binding assay on solubilized receptors

SNAP-μOR membranes were resuspended in solubilization buffer (see below for composition details) and stirred 1 hour at 4°C. After centrifugation at 36,000 g for 20 min at 4°C, the solute material was complemented with 2 mM $CaCl_2$ and loaded on M1 antibody Resin. Detergent exchange protocol was performed (see below for details) and solubilized SNAP-μOR was eluted from M1 antibody resin. Naltrexone-d2 binding affinity toward solubilized SNAP-μOR was determined at 3 nM against 0.5 nM on living cells and 1 nM HEK293 cell membranes. Freshly prepared solubilized SNAP-μOR were incubated with increasing concentrations of agonists and a fixed concentration of fluorescent naltrexone-d2 (12 nM = K_d) before HTRF signal detection.

(Met-ε)-[$^{13}CH_3$]-μOR-2x M72T expression

We generated a μ-OR mouse construct with features designed to enhance stability for NMR spectroscopy. A tobacco etch virus (TEV) protease recognition site was introduced after residue 51, and a human rhinovirus 3C protease site after residue 358. Receptor expression was largely improved by using a M72$^{1.36}$T single-point mutation as previously reported by naloxone binding (Sounier et al., 2015). A FLAG tag was added to the amino terminus and an 8 × His tag was appended to the carboxy terminus (μOR-2x). Recombinant baculoviruses were generated using the BestBac baculovirus system according to manufacturer's instructions (Expression Systems). For the assignment of all other mutants, we used the pFastBac baculovirus system (ThermoFischer). High titer baculoviruses encoding μOR-2x genes were used to infect Sf9 cells at a cell density of 4×10^6 cells per ml in suspension in methionine deficient media (Expression System) in the presence of 3 μM naloxone with ^{13}C methyl labeled methionine (Cambridge Isotope) added into the media at 250 mg·L^{-1} concentration. Cells were harvested by centrifugation 48 h post-infection and stored at −80°C until purification.

(Met-ε)-[$^{13}CH_3$]-μOR-2x M72T purification

Cell pellets were resuspended in 10 mM Tris-HCl pH 7.5, 1 mM EDTA buffer containing 2 mg·mL^{-1} iodoacetamide and protease inhibitors without salt to lyse the cells by hypotonic lysis. Lysed cells were centrifuged (38,420 g) and the membranes were solubilized durinf 1h @ 4°C using buffer containing 20 mM HEPES (pH 7.5), 200 mM NaCl, 0.5% (w/v) n-dodecyl-β-D-maltoside (DDM, Anatrace), 0.3% (w/v) CHAPS, 0.03% (w/v) choslesteryl-hemi-succinate (CHS, Sigma), 2 mg·mL^{-1} iodoacetamide and protease inhibitors. The solubilized receptor was loaded onto anti-Flag M1 column (Sigma) and washed thoroughly with DDM buffer containing 20 mM

HEPES (pH 7.5), 100 mM NaCl, 0.1% (w/v) DDM, 0.03% (w/v) CHAPS, 0.015% (w/v) CHS and 2 mM CaCl$_2$. While on the M1 antibody resin, the receptor was exchanged into lauryl maltose neopentyl glycol (LMNG, Anatrace) detergent-containing buffer composed of 20 mM HEPES (pH 7.5), 100 mM NaCl, 0.5% (w/v) LMNG and 0.01% CHS. The detergent exchange was performed by washing the column with a series of seven buffers (3 CV each) made up of the following ratios (v/v) of LMNG buffer and DDM buffer: 0:1, 1:1, 4:1, 9:1, 19:1, 99:1 and LMNG exchange buffer alone. The column was then washed with 20x critical micelle concentration (cmc) LMNG buffer containing 20 mM HEPES (pH 7.4), 100 mM NaCl, 0.02% (w/v) LMNG and 0.0004% CHS and the bound receptor was eluted in the same buffer supplemented with 0.2 mg·mL^{-1} Flag peptide. To remove flexible amino and carboxy termini, TEV and 3C protease were added at a 1:5 and 1:10 protease:µOR-2x ratio by weight. The sample was incubated at 4°C overnight in the presence of 100 µM of TCEP. We then used a negative Ni-NTA chromatography step to remove TEV and 3C proteases.

(Met-ε)-[^{13}CH$_3$]-µOR-2x M72T assignment procedure

To obtain sequence-specific assignments, we introduced single point mutations of 13 methionines in µOR by site-directed mutagenesis (Genecust). To identify suitable methionine substitutions, we performed a sequence alignment of µOR homologs and selected the most common amino acid for each position: M65T, M72T, M90I, M99L, M130L, M151I, M161I, M203I, M205L M243V, M255I, M264L and M281L. The mutants were expressed and purified as described above, except for M151I which was unstable in the detergent micelles. Ten methionines were unambiguously assigned by comparing the spectra of µOR and the µOR mutants in both *apo* and fully active states (Figure S3). M90 and M99 could not be assigned (Figure S3).

(Met-ε)-[^{13}CH$_3$]-µOR-2x M72T reductive methylation

Receptor preparation from the Ni-NTA flow through were incubated at 4°C overnight with 10 mM ^{13}C-formaldehyde and 10 mM NaBH$_3$CN. Excess of reagent was eliminated by dialysis and (Met-ε)-[^{13}CH$_3$],(Lys-Nε,Nε)[^{13}CH$_3$,^{13}CH$_3$]-µOR ((^{13}C-M^{ε},K^{me2})-µOR) was further purified by SEC chromatography in a buffer containing 0.01% LMNG, 0.001% CHS, 20 mM HEPES pH 7.4 and 40 mM NaCl. The monodisperse peak was then concentrated to 30 to 60 µM final, and dialysed in 98.85% D$_2$O buffer with 0.01% LMNG, 0.0004% CHS, 20 mM HEPES-d18 pH 7.4 (uncorrected) and 40 mM NaCl.

Nanobody Nb33 expression and purification

The Nb33 was expressed and purified as described in our previous work (Sounier et al., 2017). Briefly, The DNA sequence of Nb33 was subcloned into a pMalp2x vector containing an N-terminal, 3C protease-cleavable maltose binding protein (MBP) tag and a C-terminal 8 × His tag. Plasmids were transformed into BL21(DE3) cells and protein expression induced in liquid broth (LB) by addition of IPTG to 0.5 mM at an OD$_{600}$ of 0.6. Cells were harvested after overnight growth at 20°C by centrifugation at 6,000 g for 30 min. Cells were resuspended in 20 mM HEPES buffer (pH 7.5), 500 mM NaCl, 0.1 mg·mL^{-1} lysozyme and PMSF was added as a protease inhibitor before lysis by sonication. The cell lysate was centrifuged at 38,420 g for 30 min at 4°C. The soluble fraction was isolated and was supplemented with imidazole to a final concentration of 20 mM. MBP–nanobody fusions were purified by Ni-NTA chromatography and MBP was removed using 3C protease. Cleaved MBP was separated from the nanobody by additional amylose purification and size exclusion chromatography in a buffer containing 20 mM HEPES pH 7.4 and 0.1 M NaCl.

NMR spectroscopy

Final samples (~270 µl at 30–60 µM) were loaded into Shigemi microtubes susceptibility matched to D$_2$O. All data for ligands and mutant studies were acquired on 700 MHz Bruker Avance III spectrometers (Bruker, Rheinstetten, Germany), equipped with 5 mm cryogenic H/C/N/D probes with z axis gradient. ^{1}H-^{13}C correlation spectra were recorded using heteronuclear multiple-quantum coherence (HMQC) experiments in echo anti-echo mode. ^{13}C and ^{1}H chemical shifts and peak line widths in the HMQC spectra reveal the chemical and magnetic environments of the ^{13}C-methyl probes as well as their dynamic properties. Spectral widths in ω1 and ω2 were 8,417.5 Hz and 3,518.6 Hz at 700 MHz centered at 40 ppm or 20 ppm in the ^{13}C dimension. ^{13}C decoupling was performed with a GARP4 sequence. Typically, 134 complex points with 32–48 scans per FID were recorded, to ensure a 27-Hz resolution per point at 700 MHz before zero filling. The relaxation delay was set to 1.5 s. Thirty-two steady-state scans preceded data acquisition. Total collection time varied between 3 and 4 h, depending on the sample concentration. The spectra were visualized using CCPNMR (Vranken et al., 2005). All ligands were dissolved in perdeuterated dimethyl d$_6$-sulfoxide (d$_6$-DMSO, Cambridge Isotope) to 100 mM and directly added to the sample in the Shigemi tube at a final concentration five-fold of receptor. Nb33 were concentrated to 0.6 mM and dialysed in 100% D$_2$O buffer with 0.01% LMNG, 0.001% CHS, 20 mM HEPES-d18 pH 7.4 (uncorrected) and 40 mM NaCl. The nanobodies were added directly in the Shigemi tubes at a final concentration of two-fold of the receptor before data acquisition.

Molecular dynamics simulations

The initial coordinates of µOR were from the crystal structure of an inactive form (PDB: 4DKL). The ligands were docked to the initial µOR structure using Autodock Vina (Trott and Olson, 2010). Residues in the putative ligand-binding pocket were set flexible during docking. The protonation state of titrable residues were predicted at pH 7.4 using the H$^+$+ server (Gordon et al., 2005). The receptor-odorant complexes were embedded in a bilayer of POPC using PACKMOL-Memgen (Schott-Verdugo and Gohlke, 2019). Each system was solvated in a periodic 75 × 75 × 105 Å^3 box of explicit water and neutralized with 0.15 M Na$^+$ and Cl$^-$ ions. Effective point

charges of the ligands were obtained by RESP fitting (Wang et al., 2000) of the electrostatic potentials calculated with the HF/6-31G* basis set using Gaussian 09 (Frisch et al., 2009). The Amber 99SB-ildn (Lindorff-Larsen et al., 2010), lipid 14 (Dickson et al., 2014) and GAFF (Wang et al., 2004) force fields were used for the proteins, the lipids and the ligands, respectively. The TIP3P (Jorgensen et al., 1983) and the Joung-Cheatham (Joung and Cheatham, 2008) models were used for the water and the ions, respectively.

After energy minimization, all-atom MD simulations were carried out using Gromacs 5.1 (Van Der Spoel et al., 2005) patched with the PLUMED 2.3 plugin (Tribello et al., 2014). Each system was gradually heated to 310 K and pre-equilibrated during 10 ns of brute-force MD in the *NPT*-ensemble. The replica exchange with solute scaling (REST2) (Wang et al., 2011) technique was employed to enhance the sampling with 48 replicas in the *NVT* ensemble. REST2 is a type of Hamiltonian replica exchange simulation scheme, which performs many replicas of the same MD simulation system simultaneously. The replicas have modified free energy surfaces, in which the barriers are easier to cross than in the original system (Figure S6A). By frequently swapping the replicas during the MD, the simulations "travel" on different free energy surfaces and easily visit different conformational zones. Finally, only the samples on the original free energy surface are collected. The replicas are artificial and are only used to overcome the energy barriers. REST2, in particular, modifies the free energy surfaces by scaling (reducing) the force constants of the "solute" molecules in the simulation system. The protein and the ligands were considered as "solute"–the force constants of their van der Waals, electrostatic and dihedral terms were subject to scaling–in order to facilitate their conformational changes. The effective temperatures used here for generating the REST2 scaling factors ranged from 310 K to 700 K, following a distribution calculated with the Patriksson-van der Spoel approach (Patriksson and van der Spoel, 2008). Exchange between replicas was attempted every 1000 simulation steps. This setup resulted in an average exchange probability of ~40%. We performed 50 ns × 48 replicas of MD in the *NVT* ensemble for each system. The first 20 ns were discarded for equilibration. From our past experiences on REST2-MD of GPCR conformational changes (Cong et al., 2018, 2019; Cong and Golebiowski, 2018; Sena et al., 2017), we estimated that 50 ns should achieve millisecond timescale sampling. The original unscaled replica (at 310 K effective temperature) was collected and analyzed. Cluster analysis of the ligand binding pose was carried out on the non-restrained trajectory using the Gromacs Cluster tool. The middle structure of the most populated cluster was selected as the final binding pose.

QUANTIFICATION AND STATISTICAL ANALYSIS

For the assays described in the section "G protein activation assay," "GRK2 and GRK5 recruitment assay," "β-arrestins recruitment assay," "Internalization assay," "Fluorescent ligand-binding assay on living cells" and "Fluorescent ligand-binding assay on solubilized receptors," all experiments were conducted independently, at least three times. Data obtained were then plotted and analyzed using an operational model of agonism with GraphPad Prism Ver. 9.1.2 (GraphPad Software, Inc., San Diego, CA).

All the NMR data were processed in the same manner using NMRPipe/NMRDraw (Delaglio et al., 1995). Prior to Fourier transformation, the data matrices were zero-filled to 1024 (t_1) x 4096 (t_2) complex points and multiplied by a sine-bell window function in each dimension. Peak fitting analysis was performed with the program nlinLS (part of the NMRDraw package) using the same approach as previously described (Sounier et al., 2015). Briefly, Gaussian models were used for the fitting in each dimension, starting from values obtained from the peakpeaking routine in nmrDraw. The quality of the fits was examined visually by estimating the residual difference between the experimental data and the results of the model calculations. Peak volumes in apo-state, ligands alone and ternary complexes spectra were extracted from the peak fitting. Errors in the peak volume were calculated based on the effect of random noise for the peak height estimated by nlinLS. The peak intensities were normalized to the volume difference between the *apo* state and the ternary complex condition (DAMGO-Nb33) as the 100%.

Supplemental information

**Molecular insights into the biased signaling**

mechanism of the μ-opioid receptor

Xiaojing Cong, Damien Maurel, Hélène Déméné, Ieva Vasiliauskaité-Brooks, Joanna Hagelberger, Fanny Peysson, Julie Saint-Paul, Jérôme Golebiowski, Sébastien Granier, and Rémy Sounier

Supplemental Information

Emax (% DMAGO)	DAMGO	BU72	Oliceridine	PZM21	Buprenorphine
Gαi1	100	127 ± 17	94 ± 5	95 ± 6	63 ± 9
Gαi2	100	109 ± 8	98 ± 4	94 ± 5	66 ± 18
Gαi3	100	114 ± 14	94 ± 3	100 ± 5	83 ± 10
GαoA	100	120 ± 17	87 ± 5	90 ± 5	70 ± 5
GαoB	100	120 ± 14	91 ± 8	93 ± 9	67 ± 6
GRK2	100	98 ± 19	N.D.	N.D.	N.D.
GRK5	100	92 ± 8	N.D.	N.D.	N.D.
β-arrestin-1	100	98 ± 10	N.D.	N.D.	N.D.
β-arrestin-2	100	96 ± 12	N.D.	N.D.	N.D.
Internalization	100	96 ± 5	N.D.	N.D.	N.D.
pEC$_{50}$					
Gαi1	8.11 ± 0.13	9.76 ± 0.14	8.22 ± 0.09	8.22 ± 0.23	9.29 ± 0.77
Gαi2	8.33 ± 0.26	9.92 ± 0.24	8.59 ± 0.35	8.49 ± 0.33	8.90 ± 0.57
Gαi3	8.33 ± 0.22	9.99 ± 0.17	8.44 ± 0.05	8.51 ± 0.23	8.90 ± 0.51
GαoA	8.14 ± 0.20	9.55 ± 0.25	8.10 ± 0.09	8.12 ± 0.12	9.02 ± 0.72
GαoB	8.17 ± 0.24	10.10 ± 0.66	8.27 ± 0.32	8.25 ± 0.24	8.57 ± 0.21
GRK2	6.16 ± 0.22	8.19 ± 0.16	N.D.	N.D.	N.D.
GRK5	6.08 ± 0.13	7.65 ± 0.21	N.D.	N.D.	N.D.
β-arrestin-1	5.05 ± 0.17	8.40 ± 0.32	N.D.	N.D.	N.D.
β-arrestin-2	6.32 ± 0.12	9.00 ± 1.06	N.D.	N.D.	N.D.
Internalization	6.46 ± 0.17	8.96 ± 0.16	N.D.	N.D.	N.D.
K$_i$ (nM)					
cells	129 ± 50	0.7 ± 0.3	3.1 ± 2.5	6.7 ± 5.4	0.3 ± 0.2
Solubilized μOR	1255 ± 221	0.9 ± 0.7	66.0 ± 44.0	59.0 ± 33.0	2.3 ± 2.4

Table 1. Potency, E$_{max}$ (relative to the maximal response of DAMGO) and affinity of the five ligands in assays. Related to Figures 1 and S1.

Data presented as means ± S.D. of four to seven independent transfections performed in triplicates.
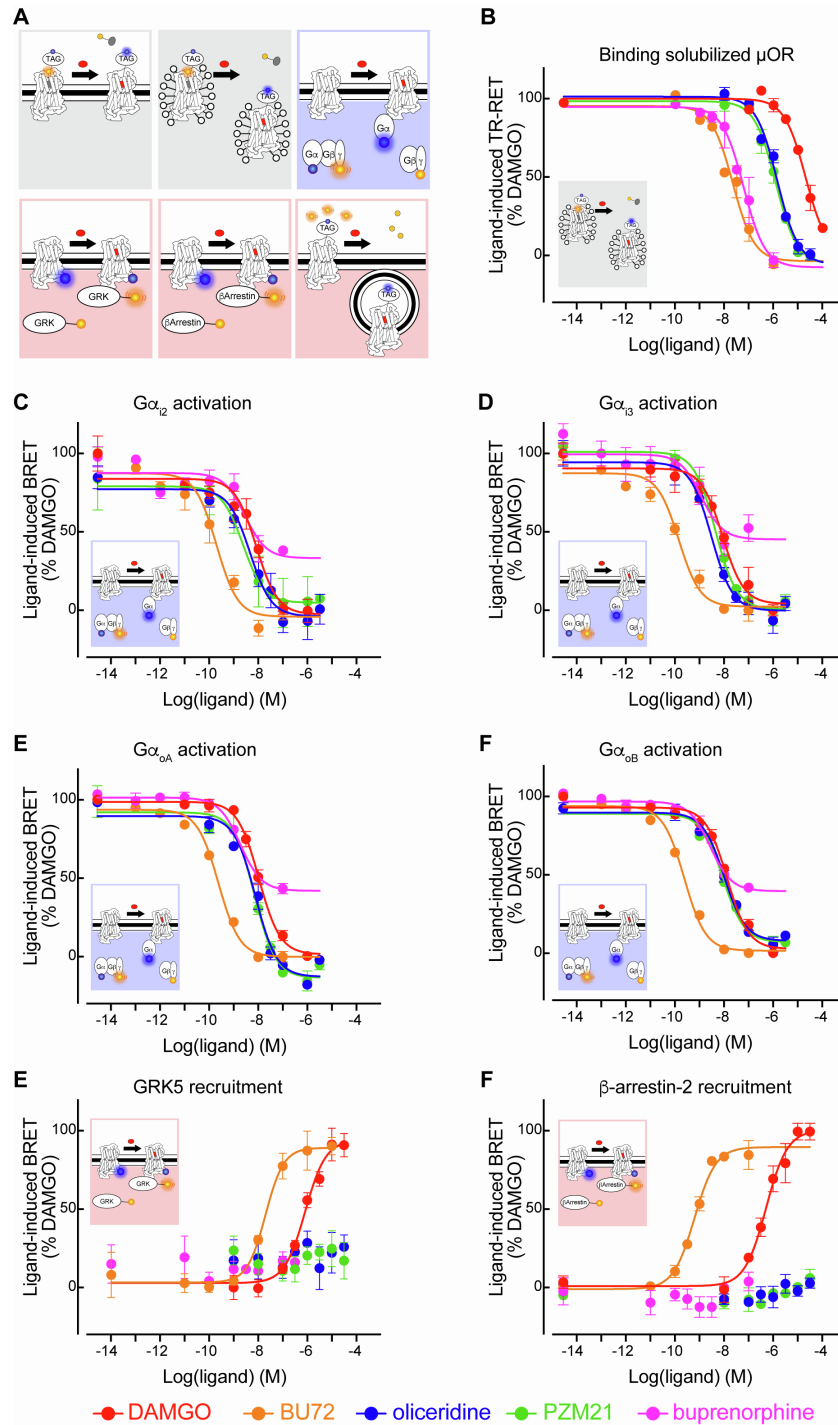
Figure S1. Functional characterization of the five ligands. Related to Figure 1.

(**A**) Schematic representation of the different BRET and TR-FRET assays used (donors are in blue and acceptors are in yellow). Dose-dependent response curves of the agonists in (**B**) competitive binding to solubilized μOR against fluorescent naltrexone, (**C**) activating Gα$_{i2}$, (**D**) activating Gα$_{i3}$, (**E**) activating Gα$_{oA}$, (**F**) activating Gα$_{oB}$, (**E**) inducing GRK5 recruitment, and (**F**) inducing β-arrestin-2 recruitment. Data shown are the means ± S.D. of a representative experiment performed in triplicates normalized to the maximal response induced by DAMGO and fitted using an operational model of agonism.
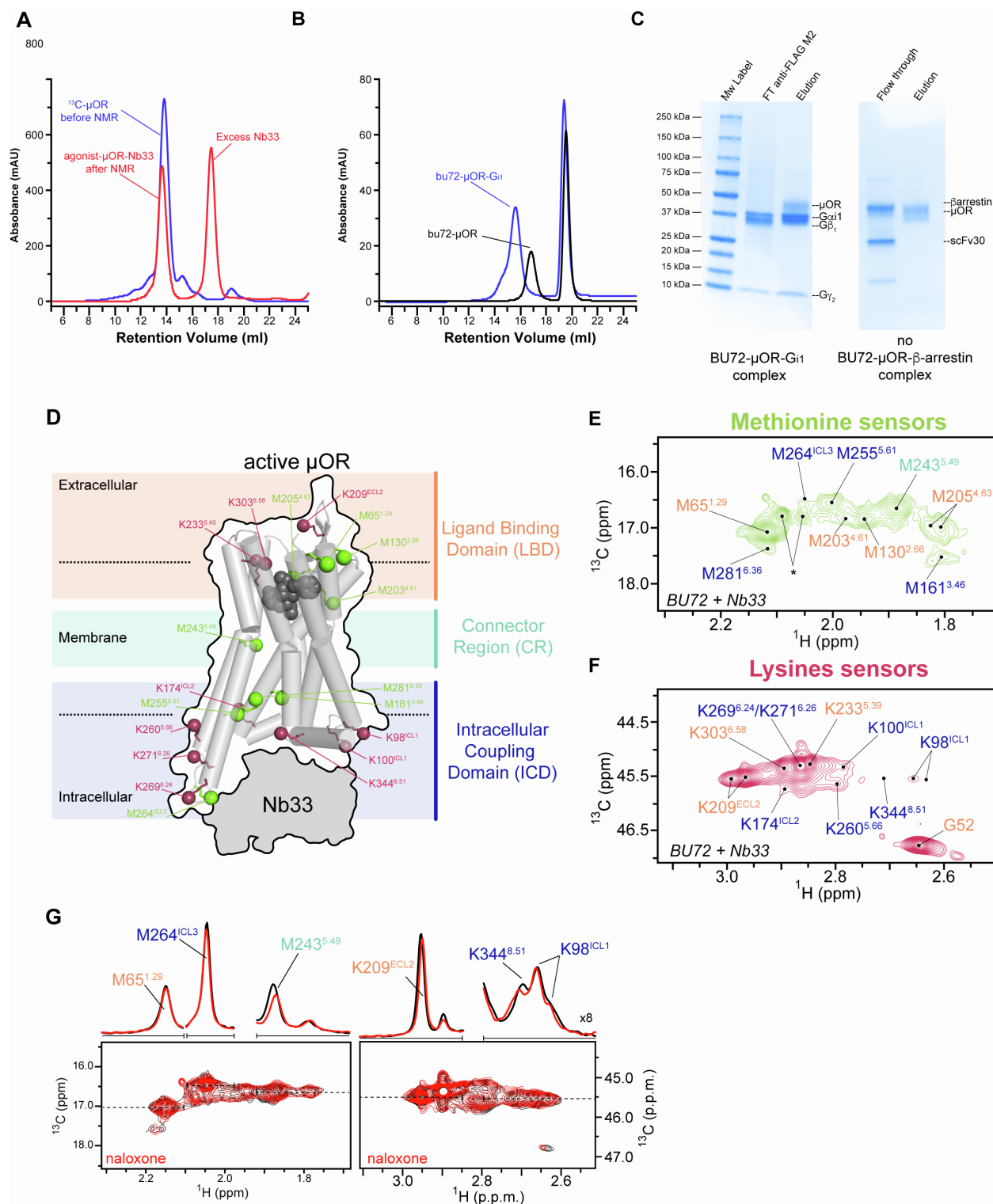
Figure S2. Biophysical characterization of μOR complexes and development of NMR sensors. Related to Figure 2.

(**A**) Typical size-exclusion chromatography (SEC) results showed the monodispersity of ^{13}C-labelled μOR (^{13}C-μOR) before NMR (Blue) and the agonist-μOR-Nb33 complex after NMR experiments (Red) using Superdex200 columns. (**B**) Typical SEC results showed the BU72-μOR-Gi complex using Superose6

columns. (**C**) SDS-PAGE of BU72-µOR-Gi1 complexes after anti-FLAG M2 resin pull-down confirmed the complex is made of µOR, Gαi1, Gβ1, Gγ2. In comparison, BU72-µOR-arrestin complexes were not observed under the same condition. (**D**) Location of the NMR sensors in a cartoon representation of the BU72-µOR-Nb33 ternary complex. NMR sensors, ε-CH$_3$ of methionine (green) and ε-NH$_2$ of lysine (raspberry), are shown in balls. (**E** and **F**) Extracted 2D HMQC spectra of the methionine and lysine sensors, as well as the backbone amine of the N-terminal residue G52, in the BU72-µOR-Nb33 ternary complex. Asterisk indicates the peak positions of residual resonances of the N-terminal methionine in a small amount of untruncated ^{13}C-µOR. (**G**) Comparison of HMQC spectra of µOR in apo-state (black) and saturating concentration of naloxone (red). 1D slices of HMQC spectra in the ^{1}H dimension is shown on top of each spectra.
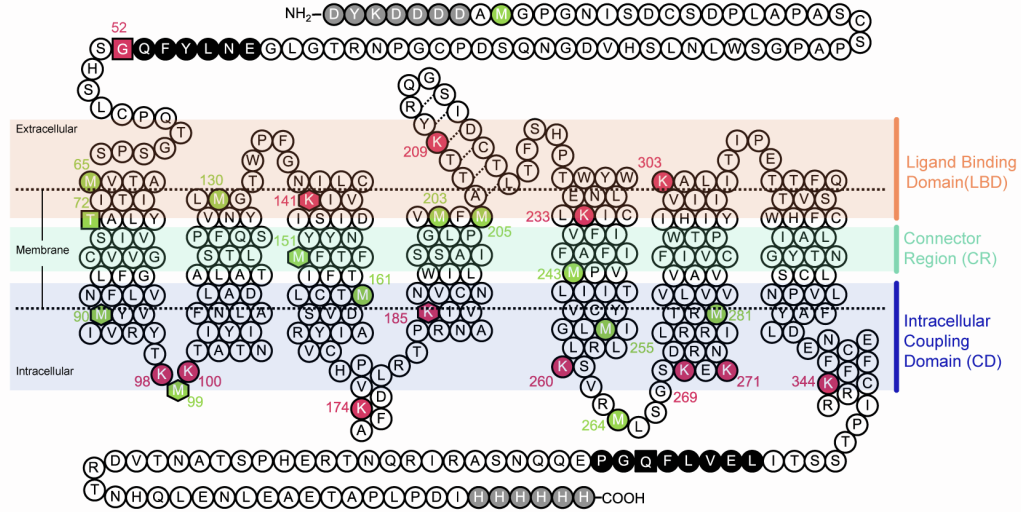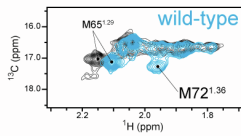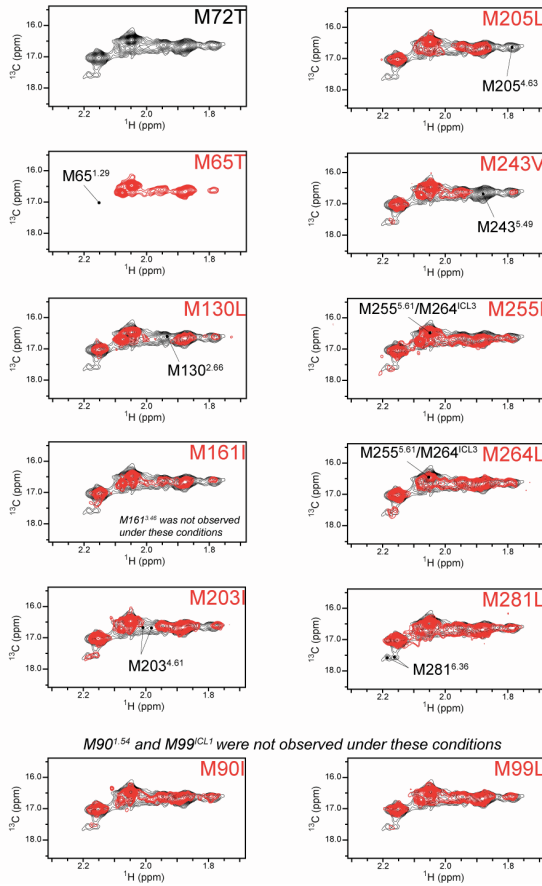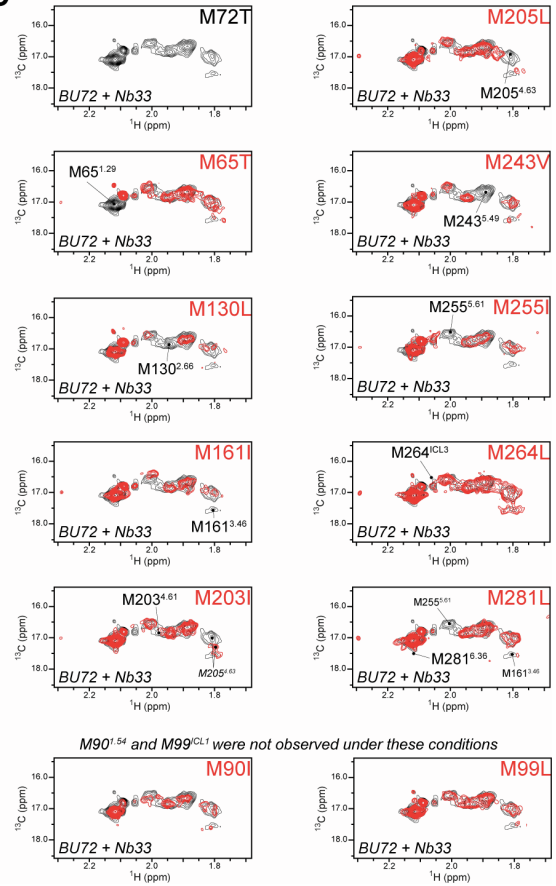
Figure S3. Assignments of resonances from methyl methionines of µOR in *apo* state and in complex with BU72 and Nb33. Related to STAR Methods.

(**A**) Snake plot of µOR sequence showing the FLAG and 6x Histidine tags (light gray), the protease cleavable motifs (black), the M72$^{1.36}$T mutation site (green, squared), as well as the methionine (green), lysine (raspberry) and G52 amine (red, squared) sensors. Unassigned residues in the 2D HMQC spectra are shown in hexagonal. (**B**) Comparison of the HMQC spectra of ^{13}CH$_3$-ε-methionine labeled wild-type µOR (blue) and µOR-M72T (black) in *apo* state. (**C** and **D**) Spectra of methionine mutants in *apo* state and in the BU72-µOR-Nb33 ternary complex. The spectra of µOR-M72T (black) was used as reference to superimpose those of the other mutants (red) We highlighted the peak disappearance for each mutant. We generated and recorded the NMR spectra for 12 mutants of 13 endogenous methionines (labeled in A). Only M151I could not be recorded because of instability issues. The spectra of M90I and M99L were not assigned under the conditions used.
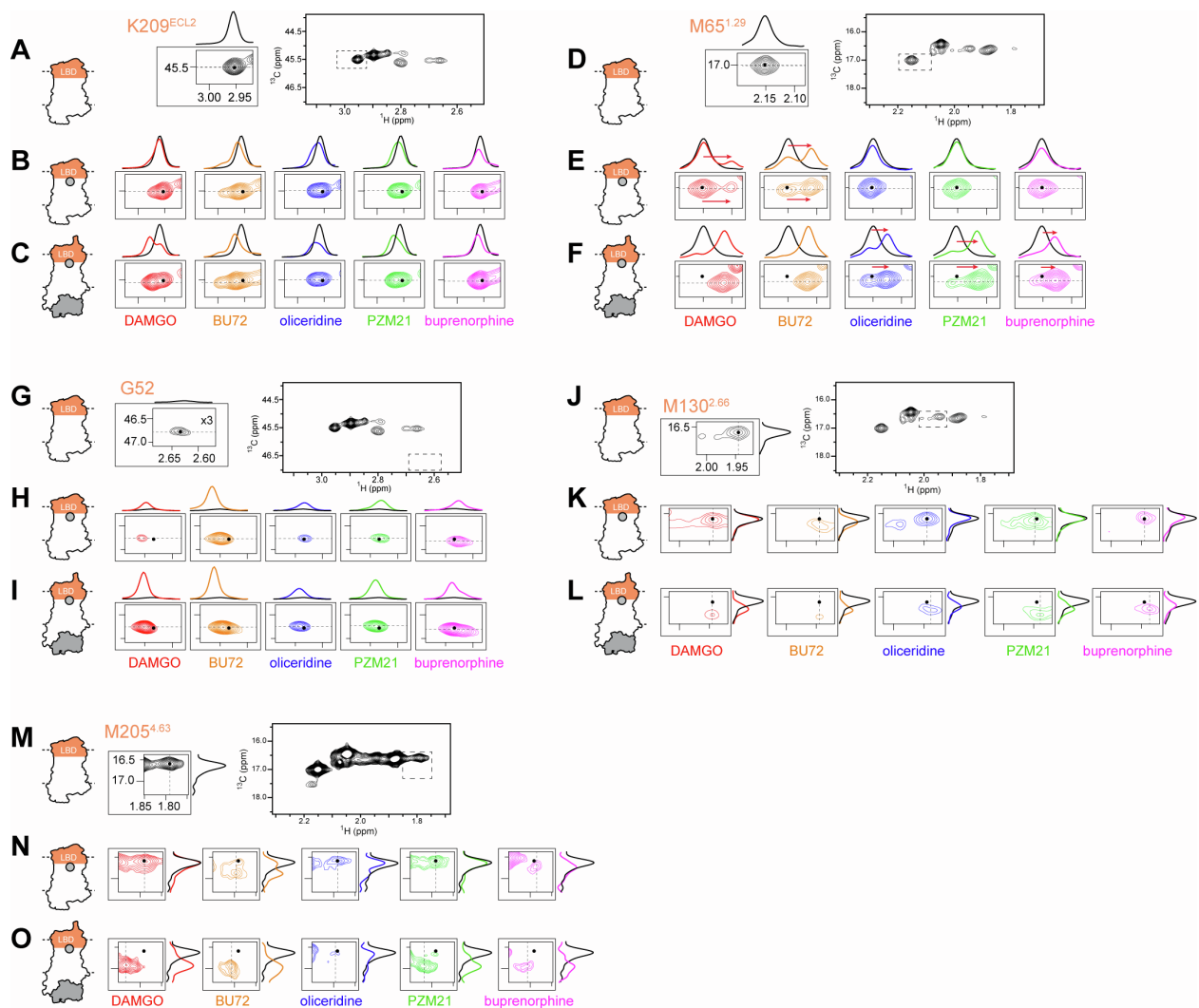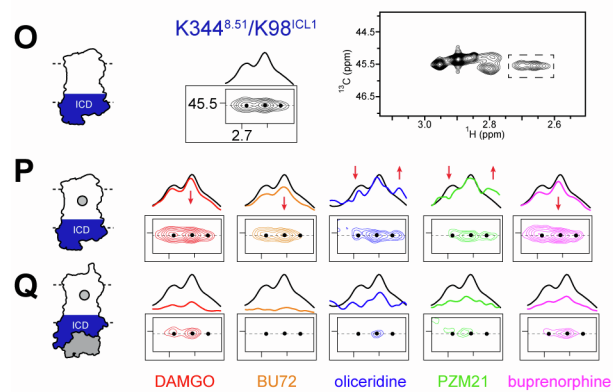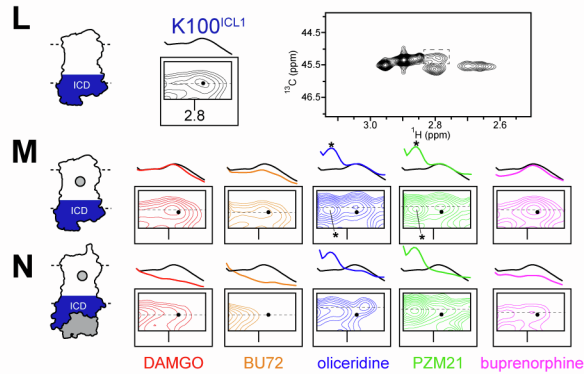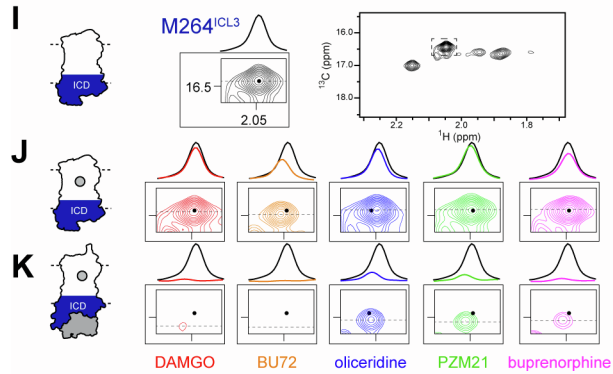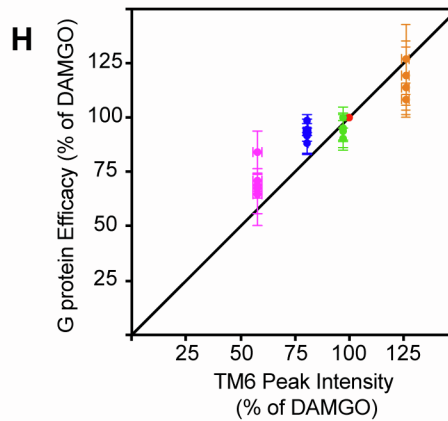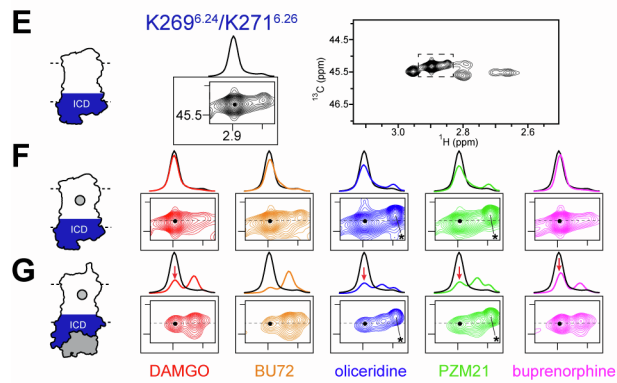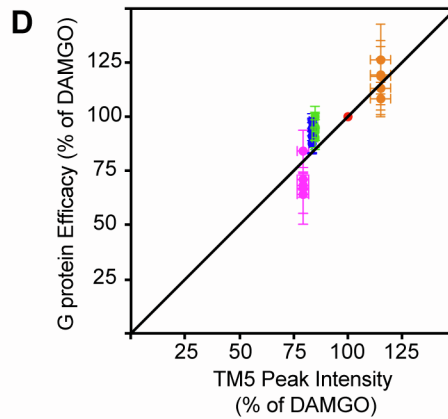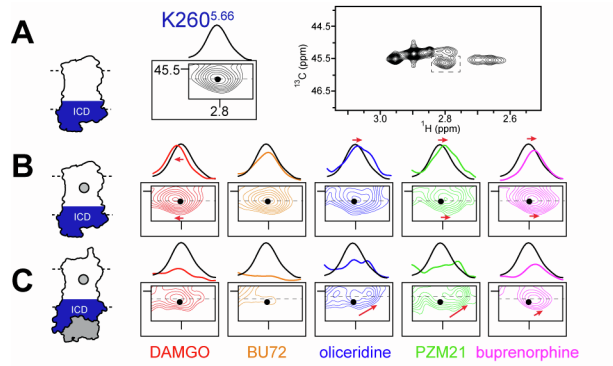
Figure S4. NMR spectral changes in the ligand-binding domain upon binding with each agonist and Nb33 at saturating concentrations. Related to Figure 3.

Extracted HMQC spectra of the sensors (**A—C**) K209^{ECL2}, (**D—F**) M65$^{1.29}$, (**G—I**) G52 amine at the truncated N-terminus), (**J—L**) M130$^{2.66}$, and (**M—O**) M205$^{4.63}$ are compared with *apo* μOR (black) (top panel), either bound to agonist (middle panel) or to agonist and Nb33 (bottom panel). Dashed black lines indicate the position of the cross-sections shown on top or on the right of the spectra.

The K209^{ECL2} (**A-B**) and M130$^{2.66}$ (**J-K**) probes only sensed slight effects of ligands alone with a decrease of signals intensity and a downfield shift of the chemical shift in the ^{1}H dimension and ^{13}C dimension. By opposition, for those two sites, Nb33 binding to the agonist-bound receptor induced important changes both in intensity and ^{1}H chemical shift for all the tested ligands (**C** and **L**). The N-terminus G52 probe sensed the binding of all ligands with a peak appearance (2.64 ppm and 46.75 ppm in ^{1}H and ^{13}C dimension) further increased in intensity upon Nb33 binding (**G-I**). These results suggest that the N-terminus of the apo form of the receptor sample more conformations than bound states. Of note, Nb33 binding at the ICD further increased the G52 methyl peak, suggesting a further stabilization of the N-terminus. Interestingly, the M65$^{1.29}$ probe revealed a ligand-specific regulation in which only BU72 and DAMGO by themselves were able to modify the chemical shift obtained in ligand free preparation (**D-F**). In particular, BU72 and DAMGO promoted the appearance of a new peak at 2.12 ppm in the ^{1}H dimension **(E)**. In the presence of Nb33, the biased ligands were able to induce a similar effect than BU72 and DAMGO alone **(F)**. However, the presence of the two peaks with different intensity suggest substantial slow conformational exchange

7

between different states. Of note the peak from the unliganded state (2.15 ppm) totally disappeared in the ternary complex samples for non-selective agonists (BU72, DAMGO). The NMR cross-peak of M205$^{4.63}$ in the HMQC spectra is highly dependent of the bound ligand. The distinct effects between agonists may be due their different chemotypes (**Figure 1A**). However, binding of ligands results in the appearance with two new close peaks at the downfield resonance in the ^{13}C dimension together with a highly broadening/splitting of the apo peak (BU72), in the increase and broadening towards downfield ^{13}C shift signal intensity (DAMGO), in the loss of signal intensity (e.g., oliceridine, buprenorphine) or no changes (e.g., PZM21) (**M**). As observed with M65$^{1.29}$, binding of Nb33 at the ICD causes more drastic changes in the NMR resonance of M205$^{4.63}$. Particularly for all agonists, we observe the appearance of multiple peaks, which shifts downfield from the apo-state peak for both ^{1}H and ^{13}C dimensions, recovering the new peak observed in the binary complex with BU72 (**O**). These observations suggest that the local conformation may become more dynamics and multiple conformations that exchange on the intermediate or slow NMR timescales.

Figure S5. NMR spectral changes on the intracellular coupling domain upon binding with each agonist and Nb33 at saturating concentrations. Related to Figure 5.

Extracted HMQC spectra of the sensors (**A—C**) K260$^{5.66}$, (**E—G**) K269$^{6.24}$/K271$^{6.26}$, (**I—K**) M264^{ICL3}, (**L—N**) K100^{ICL1} and (**O—Q**) K344$^{8.51}$/K98^{ICL1} are compared with *apo* μOR (black) (top panel), either bound to agonist (middle panel) or to agonist and Nb33 (bottom panel). Dashed black lines indicate the position of the cross-sections shown on top of the spectra. Black dots indicate the peak centers of *apo* μOR. Asterisks in (M) and (N) indicates signals from impurity most likely comes from the uncleaved N-terminus. Agonist efficacies for G proteins correlate with the changes in the peak intensities at (**D**) K260$^{5.66}$ and (**H**) K269$^{6.24}$/K271$^{6.26}$ in the ternary agonist-μOR-Nb33 complexes. DAMGO is used as reference (set at 100%). Verticals error bars indicate SEM for each of the five Gαi/o proteins (Table S1). Horizontals error bars represent the uncertainty in volume determination due to random noise.
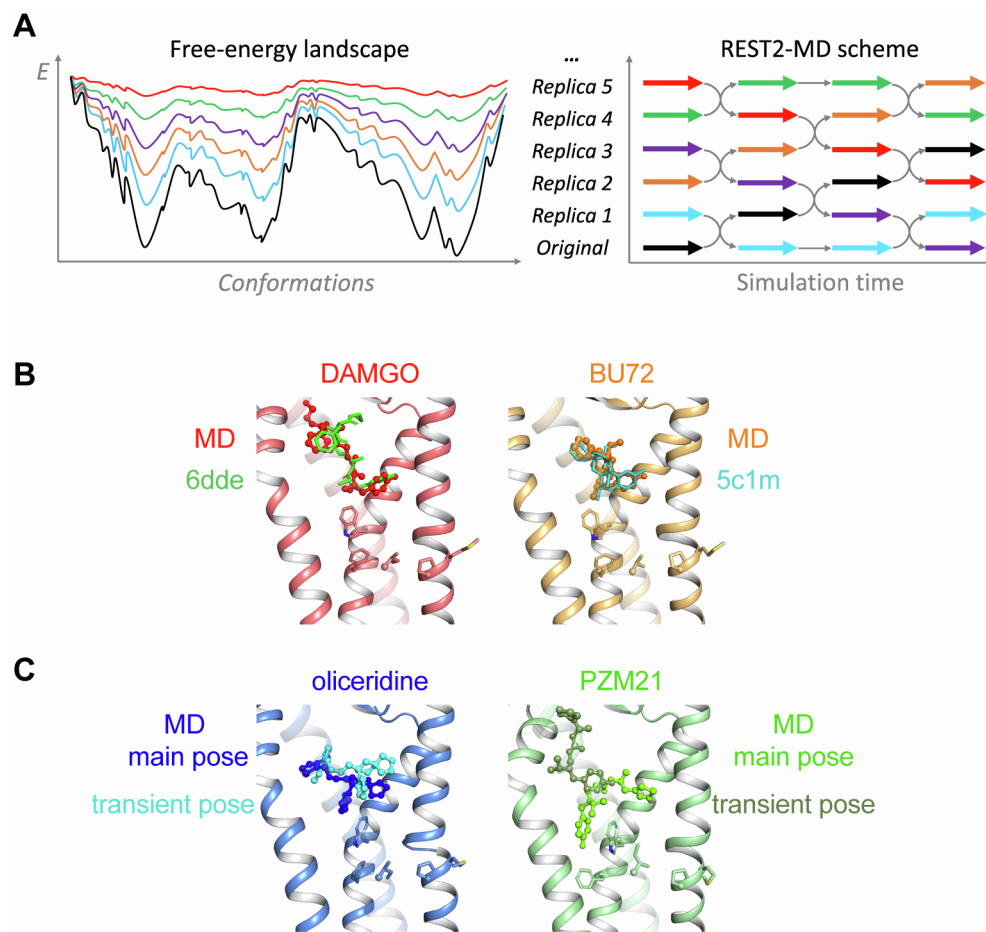
Figure S6. REST2-MD simulation scheme and ligand binding poses captured by REST2-MD. Related to STAR Methods.

(**A**) REST2-MD performs many replicas of the same simulation system simultaneously. The replicas have flatter free energy surfaces to ease barrier crossing. By frequently swapping the replicas during the MD, the simulations "travel" on different free energy surfaces and easily visit different conformational zones. (**B**) The binding poses of DAMGO and BU72 reproduced those in the experimental structures (PDBs 6DDE and 5C1M, respectively). (**C**) Transient binding poses of oliceridine and PZM21 compared with the main poses.
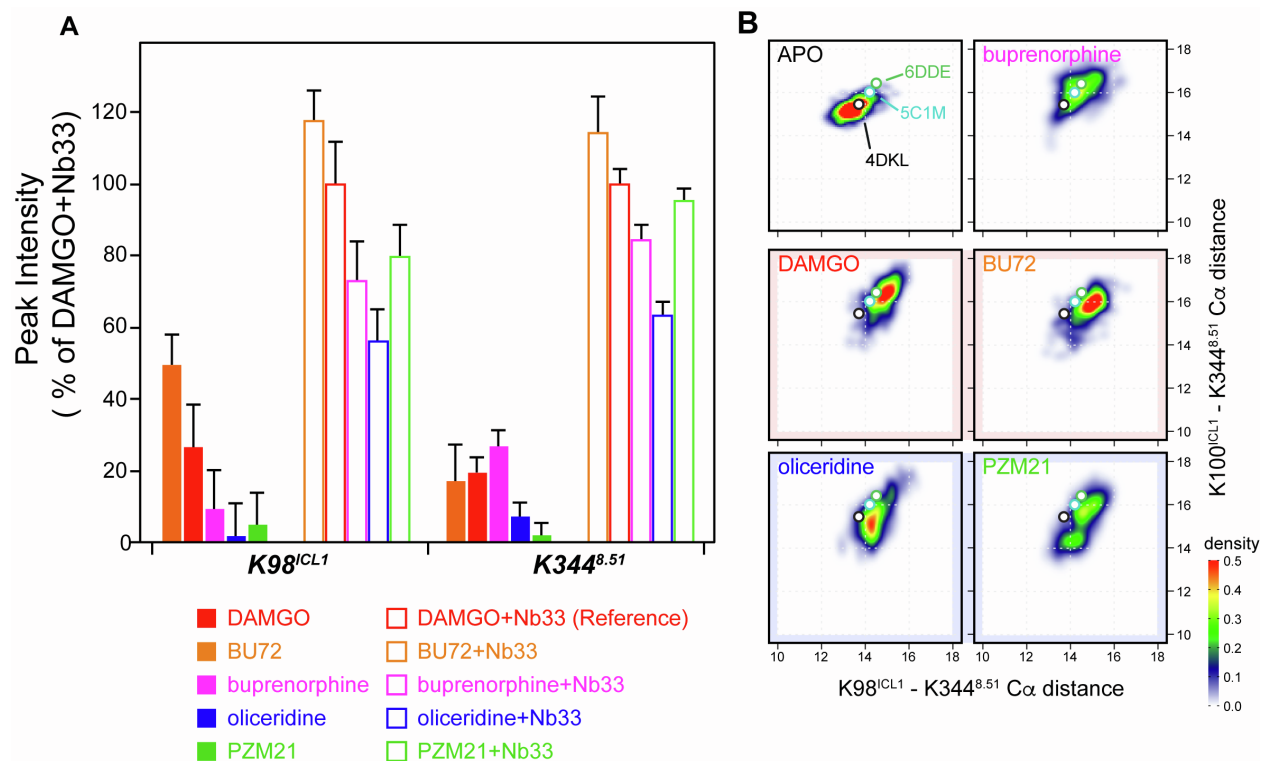
Figure S7. Conformational changes of ICL1/H8 upon binding the agonists and Nb33. Related to Figure 5.

(**A**) Peak intensities were normalized to the volume difference between the *apo* state and DAMGO-µOR-Nb33 ternary complex as the 100%. Error bars represent the uncertainty in volume determination due to random noise. (**B**) Density maps of the Cα distances between K98^{ICL1}, K100^{ICL1} and K344$^{8.51}$ during REST2-MD of the agonist-µOR-Nb33 ternary complexes, compared with the *apo* state and the values in experimental structures ((PDBs 4DKL, 6DDE and 5C1M).